NO measurements in high temperature hydrogen flames: The crucial role of the hydrogen oxidation chemistry for accurate NO predictions

Marie Meulemans[a], Antoine Durocher[a,b], Gilles Bourque[a,c], Jeffrey M. Bergthorson[a]

[a] *Alternative Fuels Laboratory, McGill University, 817 Sherbrooke St W, Montréal, H3A 0C3, QC, Canada*
[b] *Gas Turbine Laboratory, National Research Council of Canada, Ottawa, K1K 2E1, ON, Canada*
[c] *Siemens Energy Limited, 9545 Chemin de la côte de Liesse, Dorval, H9P 1A5, QC, Canada*

Abstract

The current work investigates the formation of Nitric Oxide (NO) in hydrogen-air flames, over a wide range of flame temperatures. The use of hydrogen allows improved focus on the thermal-NO pathway by removing the complexity introduced by the prompt-NO pathway, which has been shown to be an important contributor to inaccurate predictions of absolute post-flame NO concentrations in hydrocarbon flames. This experimental study is conducted at atmospheric pressure using stoichiometric, premixed, laminar stagnation flames. Adiabatic flame temperatures ranging from 1600 K to 2300 K are achieved by varying the argon concentration in air. One-dimensional velocity, temperature, and NO concentration profiles are measured using non-intrusive laser diagnostics: Particle Tracking Velocimetry (PTV), NO multiline thermometry, and NO Laser Induced Fluorescence (NO-LIF), respectively. Results show that the experimental velocity profiles are incorrectly captured by the studied mechanisms, especially at low and high temperatures. This suggests that major inaccuracies are present in the hydrogen oxidation chemistry of the thermochemical models, regardless of their optimisation methodology. Furthermore, NO-LIF profiles show major discrepancies between all the studied mechanisms and the experiments, especially at elevated temperatures. The disagreement stems from an inaccurate description of the base chemistry of the models. These inaccuracies arise specifically from the description of the radical pool driving the flame behaviour and NO formation. This study demonstrates the need for model optimisation on experimental measurements using pure hydrogen 1D flames to obtain an accurate description of the hydrogen oxidation chemistry at play. This would lead to an improved description of the NO_x sub-chemistry of any hydrogen, or hydrocarbon, combustion system.

Keywords: Chemical kinetics, Hydrogen, Nitric oxide, NO pathways, NO-laser induced fluorescence, Premixed flame

Novelty and significance statement

This work presents an in-depth analysis of experimental results to understand the origin of significant discrepancies observed between state-of-the-art combustion models and the experimental results. This study provides a unique experimental data set comprising of velocity, temperature, and NO concentration measurements in low- to high-temperature 1D hydrogen flames. NO measurements in hydrogen combustion, particularly spatially- or temporally-resolved, are scarce in the literature and is of high-value for the modelling community. In addition, this study provides detailed analyses that illustrates the source of major mispredictions in velocity and NO concentration measurements between the experimental and numerical results. These inaccuracies appear to stem from the core hydrogen-oxidation chemistry, fundamental in the description of any combustion process involving hydrogen and hydrocarbon fuels. This work aids the modelling community in its efforts to further improve the predictive capabilities (kinetics, speciation, thermodynamics) of combustion models, and is key for the minimisation of emissions of alternative fuels in practical applications.

Author contributions

Marie Meulemans: designed and conducted experiments and simulations, analysed and interpreted results, drafted, revised, and edited the manuscript. **Antoine Durocher:** contributed to the analysis and interpretation of the results, revised the manuscript. **Gilles Bourque:** co-supervised the research, revised the manuscript. **Jeffrey M. Bergthorson:** supervised the research, revised the manuscript and approved of the final version that was submitted.

1. Introduction

As industries are transitioning from fossil fuels to more sustainable, carbon-free fuels, such as hydrogen, the interest in Nitric Oxide (NO) formation is growing, and accurate modelling is required as a design tool. Constant efforts have been spent over the last few decades to accurately model NO_x chemistry through the different NO-formation pathways.

Glarborg et al. [1] formalised these efforts to validate a new comprehensive nitrogen chemistry model. They not only reviewed the two most important pathways of NO formation in flame conditions, prompt-NO and thermal-NO, they also emphasised the less dominant pathways, N_2O and NNH, and their

inter-dependencies to one another. The importance of these two minor pathways is increasing as industries target operating conditions that mitigate the prompt-NO and thermal-NO pathway contributions [2, 3].

Extensive work has been conducted to precisely model these four pathways. The prompt-NO pathway, one of the most important sources of NO in hydrocarbon combustion, occurs through the reaction of CH with N_2 to form NCN+H [4, 5]. The further reaction of NCN leads to NO formation through reactions with the radical pool. Efforts to model each reaction of the prompt-NO subset are still underway [6–9].

The thermal-NO pathway, another important source of NO formation, occurs through the reaction of N_2 with O to form NO+N [10]. This reaction is the rate limiting step due to its high activation energy. Thermal-NO pathway is highly dependent on temperature and residence time and is, generally, the main source of NO formation in practical systems, such as gas turbines. Therefore, this pathway is extensively studied, as it is generally limited to the study of a single reaction instead of a subset of reactions [11–14].

The N_2O pathway consists of the oxidation of N_2 with O to form N_2O [15]. The further reaction of N_2O with the radical pool leads to NO formation. The formation conditions of this pathway, in lean flames at moderate temperatures and high pressures, makes it relevant to practical combustion systems, such as Dry Low Emission (DLE). Yet, this subset of reactions still has limited data as it is not as dominant as the previous two pathways. This is in part due to the fact that this pathway is predicted to be dominant only at high pressures, and thus presents experimental challenges to perform laser-based diagnostics to characterise it. Nevertheless, the interest in this pathway is growing as its contribution increases with the use of emission-reduction strategies and the reduction of the contribution of previously dominant pathways [16–19].

Similar to the N_2O pathway, the NNH pathway is the reaction of N_2 with H to form NNH [20]. NO is formed through the reaction of NNH with the radical pool. This subset of reactions is the least studied in the literature as it is rarely dominant in combustion systems [21–23]. With the advent of sustainable fuels, especially hydrogen, this pathway could see its contribution growing with a greater availability of H-atoms through H_2 breakdown and the absence of the prompt-NO pathway.

Recently, Lee et al. [24] and Meng et al. [25] have presented a new potential formation channel through the HNNO intermediate. This pathway appears to be active at low temperatures and moderate to elevated pressures. This discovery implies that some models would not accurately describe NO formation as they have, so far, been optimised accounting for only 4 pathways.

Despite all these efforts to precisely model each pathway involved in NO formation over a wide range of flame conditions, inaccuracies remain in the understanding of its chemistry [14, 17, 26–29]. In several experimental and numerical studies targeting the prompt-NO pathway in short-chain hydrocarbon flames [26, 28, 30], it was demonstrated that an inaccurate description of the radical species, especially CH, O, and H, leads to misprediction of the NO chemistry in the flames. Similarly, experiments in high-pressure hydrogen flames [29], targeting the N_2O and the NNH pathways, have shown large variability in the prediction capability of different models. The dependence of these pathways with the co-reacting radicals O, H, and OH, could lead to mispredictions of NO concentration if they are not modelled adequately. Furthermore, Meulemans et al. [14] have shown that models are not able to accurately capture the NO chemistry in methane-air flames, particularly at high temperatures where thermal-NO is most active. They concluded that the discrepancies observed are likely due to an inaccurate description of the base chemistry of the thermochemical models employed, as well as an inaccurate description of the NO formation pathways, specifically their reaction rates and the pathway inter-dependencies.

These studies suggest that a significant gap remains in the understanding of NO formation pathway description and their interaction with one another, independently of the fuel used. A strong dependency is also demonstrated between the pathway prediction accuracy and the adequate modelling of the radical pool concentration by the models. These modelling inaccuracies in the formation pathway rates or in the radical pool formation would hinder the accurate prediction of NO formation in conditions that approach practical applications.

Recent measurements in atmospheric, lean-to-rich, hydrogen flames [31] interrogates the accuracy of the radical pool modelling by thermochemical models. They found that large discrepancies are observed between measurements and predictions of the laminar flame speed of 8 lean-to-rich hydrogen flames. This study demonstrates that inaccuracies in the kinetic performance of existing models for hydrogen oxidation. This finding is concerning as it suggests that the hydrogen oxidation modelling remains inaccurate. Indeed, the hydrogen oxidation chemistry is the first, and most important, building block of any combustion model [32]. It is only composed of a limited set of reactions and species (generally around 30 and 10, respectively), but its description is paramount to an accurate description of any combustion property (kinetics, thermodynamics, speciation).

Thermochemical models, especially those built in a hierarchical manner, are expected to perform well in this first building block, as they individually optimise the hydrogen oxidation chemistry on relevant dataset (directly, indirectly, or *ab initio*). Nevertheless, this review of recent experimental studies indicate that this assumption may not hold true, the description of the NO chemistry remains mispredicted in most conditions presented. This could be explained by the fact that most models, when optimising their NO_x sub-chemistry, generally include data from non-flame setup (shock tube, flow reactor), as well as a range of dataset from both hydrogen and hydrocarbon combustion. Therefore, a misunderstanding of the radical pool description in such contexts could lead to a mis-optimisation of the NO_x chemistry subset. An improvement in modelling accuracy could be gained by including more hydrogen experimental datasets generated from relevant flame conditions. Unfortunately, relatively few experiments have been performed using pure hydrogen flames, especially those that measure NO formation [3, 17, 29, 33–36]. Therefore, the use of pure hydrogen

fuel stretches these models into conditions where they have little validation data, possibly propagating the existing errors in NO predictions of hydrocarbon flames when employed to predict NO formation in hydrogen flames. As a consequence, hydrogen flames should be employed to validate any hierarchical models regarding NO measurements, as well as velocity measurements.

To address the lack of hydrogen flame data, this study provides a dataset of velocity, temperature, and NO concentration measurements in pure hydrogen flames. Nine atmospheric, premixed, laminar, stoichiometric, hydrogen-air flames are studied using a stagnation flame burner. Adiabatic temperatures ranging from 1600 K to 2300 K are achieved using argon dilution to emphasise the thermal-NO pathway. The resulting dataset is compared to the modelling capability of several recent and commonly-used thermochemical models. These conditions have been chosen to provide a robust set of data fit for model optimisation and validation. The use of hydrogen focuses on the first building block of any hierarchical thermochemical model. In addition, it allows the removal of the contribution of the prompt-NO formation pathway, a source of misprediction in previous studies. Furthermore, the use of elevated temperatures challenges the models in extreme conditions, outside of their traditional validation range. Models that perform well in these conditions are more likely to have been built in a robust manner, as they capture the fundamental behaviour of the relevant reactions.

2. Experimental methods

2.1. Stagnation burner

Atmospheric, stoichiometric, premixed hydrogen-air-argon flames are obtained using the jet-wall stagnation flame burner shown in Fig. 1. This setup provides accurate boundary conditions allowing the performance of 1D simulations [37]. The premixed laminar flow exits the nozzle and impinges on a water-cooled stagnation plate maintained at a constant temperature during the experiment. The nozzle-to-plate distance is ~ 9 mm, and the flame is stabilised approximately at a third of the domain for each experiment in order to maximise the post-flame region, while retaining accurate velocity boundary conditions. The use of nitrogen as a coflow shields the flame from reacting with ambient oxygen. This setup provides flat, lifted, quasi-1D, stretched flames that are minimally affected by the burner. It is ideal for performing optical diagnostics, similar to previous work [14, 18, 27–29, 31, 38].

Adiabatic flame temperatures ranging from 1600 K to 2300 K are used to span a large range of temperatures used in practical systems and promote the formation of thermal-NO at higher temperatures. These temperatures are achieved by producing nine stoichiometric hydrogen-air flames diluted with different levels of argon, such that argon concentration defined by Eq. (1) varies between 62.81% at 1600 K and 12.05% at 2300 K in the oxidizer stream with:

$$X_{\mathrm{Ar}} = \frac{N_{\mathrm{Ar}}}{N_{\mathrm{O_2}} + N_{\mathrm{N_2}} + N_{\mathrm{Ar}}}, \qquad (1)$$

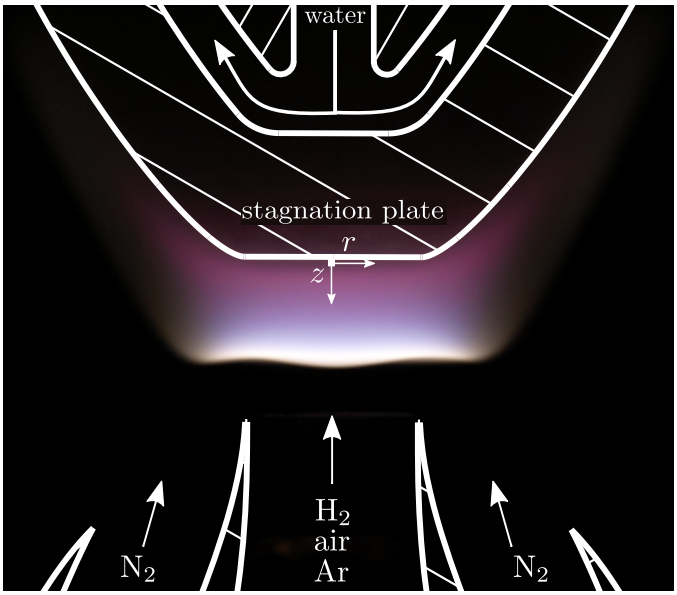

Figure 1: Stagnation flame burner displaying a stoichiometric hydrogen-air-argon flame at $T_{\mathrm{ad}} = 2100$ K using an exposure time of 4 s. The red and white hues result from H_2O and OH emissions respectively [39].

where N_i is the molar concentration of species i. Non-diluted flat flames with temperatures beyond 2300 K could not be stabilised due to intrinsic flame instabilities. The use of argon as a diluent to control the flame temperature is intentional. This enables the equivalence ratio and the oxygen-to-nitrogen ratio to remain constant while the adiabatic flame temperature varies. It is also a common bath gas in shock tubes studies and, therefore, its use in this study reduces the impact of third body reaction uncertainty due to the familiarity of its behaviour to common thermochemical models.

The different gas flow rates are controlled using thermal mass flow controllers. They are calibrated before the experiments using their respective gases with a DryCal ML-500 dry-piston calibrator, leading to an uncertainty of $\pm 0.7\%$ on the equivalence ratio and $\pm 0.85\%$ on the argon concentration.

Boundary conditions, necessary to perform simulations, are acquired during the experiments through post-processing of the velocity measurements. Type-k thermocouples are used to measure the inlet temperature of the mixture (T_{in}) and the stagnation plate temperature (T_{wall}) within ± 2 K and ± 5 K, respectively. The length of the domain used for simulations (l) is determined at the location of minimum uncertainty in the unburnt region of the velocity profiles, and is also where the inlet velocity (u_{in}) and the axial strain rate $(\mathrm{d}u_{\mathrm{in}}/\mathrm{d}z)$ are extracted [40]. This dataset can be found in the Supplementary Materials Section 1.

2.2. Velocity measurements

Velocity profiles are obtained using Particle Tracking Velocimetry (PTV). The flow is seeded upstream of the nozzle with $\sim 1\,\mu$m inert alumina particles illuminated by a 527 nm laser beam. The beam is focused on the center of the nozzle and is stretched to cover almost the entirety of the nozzle-

to-plate region. The laser is triggered at a frequency varying from 5 kHz to 10 kHz according to the velocity of the flow. The laser light scattered on the alumina particles is captured using a Charge-Coupled Device (CCD) camera set on a long exposure from 120 ms to 20 ms according to the frequency of the laser. A set of 1,200 images is obtained for each flame on which the tracer particle positions are tracked using an automated streak detection algorithm [41]. The processing of the images allow the extraction of the particle velocity profile along the centerline of the nozzle using a second-order central finite difference scheme:

$$u_{\mathrm{p}}\left(z_{\mathrm{p},i}, r_{\mathrm{p},i}\right) \approx \frac{z_{\mathrm{p},i+1} - z_{\mathrm{p},i-1}}{2} \cdot f \cdot C, \tag{2}$$

at the particle location $z_{\mathrm{p},i}$ and $r_{\mathrm{p},i}$, and with f defined as the laser frequency in Hz, and C the camera calibration coefficient in mm/pixel. The particle velocity measurements are performed twice for each flame to ensure repeatability and reach low uncertainty. The direct comparison of the simulated and measured velocity profiles are performed in the measurement unit as suggested by Connelly et al. [42]. Therefore, the simulated gas velocity profiles are converted to particle velocity profiles through the estimation of the particle drag and motion in the flow through the modelling of thermophoretic forces, particle inertia, and the finite particle-track interval effects [43].

2.3. NO concentration measurements

NO concentration profiles are obtained using two dimensional NO Laser Induced Fluorescence (NO-LIF). A wavelength-tunable dye laser, using a solution of Coumarin 450, is pumped by a Nd:YAG laser to excite NO molecules in the A-X (0,0) electronic system at a wavelength of ∼226 nm, comprising of the $P_1(23.5)$, Q_1+$P_{21}(14.5)$, and Q_2+$P_{12}(20.5)$ transitions. The fluorescence of the NO molecules going from the excited state to the ground state is captured using an Intensified-CCD (ICCD) camera equipped with a 235 nm long-pass filter to remove Rayleigh scattering and reflections. To enhance the signal-to-noise ratio, a 120 ns gate is used to reduce the noise contribution from the flame chemiluminescence. The image is binned 4×8 (vertically and horizontally, respectively) to enhance the signal while only minimally compromising the spatial resolution. Finally, 50 individual illumination events are aggregated by the camera, before readout, to enhance the fluorescence signal on single images. The axially-resolved signal of NO produced by the flame (F_{NO}) is captured using 10,000 laser pulses at two different wavelengths: at $\lambda_{\mathrm{on}} = 226.0345$ nm, to capture the online signal (S_{on}) corresponding to a maximum excitation state of the molecules, and at $\lambda_{\mathrm{off}} = 226.0470$ nm, to capture the offline signal (S_{off}), corresponding to a minimum excitation state of the NO molecules. The subtraction of the two signals results in a signal free of interfering LIF and scattering signals. The signal of the flame without laser illumination $\left(S_{\mathrm{bckg}}\right)$ is also captured using 100 images. The subtraction of the latter to S_{off} and S_{on}, removes the effect of the remaining flame chemiluminescence, camera dark noise, and ambient luminosity. The laser energy is measured close to the flame using a photo-detector, and ensures that the measurements are performed in the LIF linear regime. The signal obtained from fluorescence is normalised by the measured laser energy $E_{\mathrm{L,on}}$ and $E_{\mathrm{L,off}}$, such that the signal is proportional to the NO density only. Finally, the signal is corrected for spatial inhomogeneity in the laser sheet, obtained in a cold jet flow of NO. Under linear LIF, the normalised NO signal can be expressed by Eq. (4):

$$F_{\mathrm{NO}} = \frac{\left(S_{\mathrm{on}} - S_{\mathrm{bckg}}\right)}{E_{\mathrm{L,on}}} - \frac{\left(S_{\mathrm{off}} - S_{\mathrm{bckg}}\right)}{E_{\mathrm{L,off}}}, \tag{3}$$

$$= f_{\mathrm{LIF}}\left(f_{\mathrm{B}}, \lambda, \Delta\nu_{\mathrm{L}}, \Gamma, B_{12}, A_{21}, Q_{21}\right) \cdot C_{\mathrm{opt}} \cdot n^{\circ}_{\mathrm{NO}}\left(T, p, X_{\mathrm{NO}}\right), \tag{4}$$

where f_{LIF}, obtained using LIFSim [44], is the number of photons emitted per unit molecule of NO, per unit volume, and per laser energy,and is a function of; $f_{\mathrm{B}}(T)$ the Boltzmann fraction of NO molecules in the excited state, λ the laser wavelength, $\Delta\nu_{\mathrm{L}}$ the spectral width of the laser, $\Gamma\left(\Delta\nu_{\mathrm{L}}, T, p, X_i\right)$ the dimensionless overlap fraction, A_{21} and B_{12} the Einstein coefficients for spontaneous emission and photon absorption, respectively, and $Q_{21}\left(T, p, X_i\right)$ the rate constant of non-radiative collisional quenching. C_{opt}, obtained experimentally, is the optical calibration coefficient accounting for optic transmissivity and camera sensitivity, and n°_{NO} is the number density of NO molecules, directly proportional to the concentration of NO in the flame.

C_{opt} is obtained through calibration by measuring the signals of both an NO-seeded and unseeded flame. The difference in signals is only proportional to the NO seeded in the flame, and is independent of the NO produced by the flame. Therefore, C_{opt} can be applied on all flames of the experimental campaign, despite individually producing different levels of NO. This method is valid as long as there is negligible NO reburn or recombination within the flame, and that the seeded molecules do not significantly affect the flame properties. The methodology is further detailed in Supplementary Materials Section 2.

In order to model f_{LIF}, the knowledge of instantaneous quenching species concentrations and temperature throughout the domain is required. Thus, transforming experimental NO-LIF signals to NO concentrations relies on assumed profiles which might induce further uncertainty in the reported measurements if the assumptions and models used are proven inaccurate [42]. Therefore, to improve the comparison between measurements and simulations, simulated NO concentration profiles are transformed through LIFSim [44], a three-level LIF model, to obtain simulated NO-LIF profiles, which are directly comparable to C_{opt}-normalised experimental NO-LIF profiles. Consequently, the NO concentration profiles presented in this study are reported through $F_{\mathrm{NO}}/C_{\mathrm{opt}}$ in arbitrary units [a.u.], a combination of power and length units. The measurements of NO-LIF profiles are conducted twice, and the measurement of C_{opt} is performed 8 times. This ensures repeatability in the measurements and leads to low experimental uncertainty. Further details of the uncertainty calculation is given in the Supplementary Materials Section 4.

To accurately transform the NO-LIF signals into ppm, an uncertainty calculation of the LIF modelling parameters would be required. Despite this, for improved context, an estimate of the NO concentration is also given on the NO-LIF profiles. This

estimate is obtained by comparing the modelled NO-LIF signal of a reference mechanism to its NO concentration prediction in ppm, achieving a conversion [a.u. → ppm]. This conversion is applied to the other simulated NO-LIF profiles, as well as on the experimental NO-LIF profiles, and is mainly valid in the post-flame region of the profiles presented.

2.4. Temperature measurements

Temperature profiles are obtained using multi-line NO-LIF thermometry [45–47]. The technique uses a similar methodology as for NO concentration measurement. The flames are seeded with 200 ppm to 500 ppm (high temperature to low temperature flames, respectively, to enhance signal-to-noise ratio) of NO to track the emitted fluorescence across the entire domain. The laser wavelength is varied from 225.13 nm to 225.19 nm over 120 discrete wavelengths. The NO fluorescence is captured at each wavelength by the ICCD camera for a hardware accumulation of 80 images at 300 ns exposure, using the same technique as in a previous study [14]. However, this technique proved not adapted for high temperatures hydrogen flames due to a low signal-to-noise ratio and temperature sensitivity. Therefore, for flames with T_{ad} >2000 K, the image is binned 4×8 (vertically and horizontally, respectively). This allows the reduction of the exposure time to 120 ns, limiting the noise from flame chemiluminescence and improving the signal-to-noise ratio of high temperature flames. In order to avoid over-exposure of the photo-detectors, the image accumulation on the camera is limited to 40 images. The signal is also obtained for an unseeded flame and a flame without laser illumination. These signals are subtracted from the signal of the seeded flame, to maximise the signal-to-noise ratio. The resulting signal is representative of the fluorescence spectra of NO at each point of the domain, and is compared through a spectra-fitting procedure [45] to NO-LIF excitation spectra obtained from LIF-Base [48] in order to determine the temperature of the NO-fluorescing molecule. A 1D temperature profile, with an uncertainty of ± 5%, is extracted at the centre-line of the nozzle and is directly compared to the simulated profiles.

2.5. Flame simulation and thermochemical models

Simulations of the experimental flames are performed using the Impinging Jet model in Cantera 2.5.1 [62]. The multi-component transport model is used, and the radiation and Soret effects are included. Simulations are converged to reach refinement criteria of 2, 0.03, and 0.03, for ratio, curve, and slope respectively, and until the reference flame speed varies by less than 0.1% between each iteration of the refinement criteria. This leads to solutions containing ∼400 grid points, with a 1 μm minimum grid size. Eleven thermochemicals models are used to simulate the flames, and are presented in Tab. 1.

Three of these mechanisms; ELTE, KON, and TUM; do not possess a NO_x chemistry as they are optimised solely for hydrogen oxidation. Therefore, their simulations will only be used for the velocity analysis. The remaining eight mechanisms have been developed for fuels heavier than hydrogen. In order to simplify and minimise simulation time, they have been stripped of their carbon chemistry.

Other than stripping the thermochemical models of their carbon chemistry (or as detailed later in this paper, stripped of their NO_x chemistry), the mechanisms are not modified. Therefore, the third-body collision factors remained as they have been specified in the mechanisms. If not specified, a default value of 1 is used.

It is worth mentioning that none of the mechanisms used in this study have implemented the potential new HNNO formation pathway. This pathway is also excluded from the analysis performed later in the paper, regarding the formation of NO through the different pathways active in these conditions. This pathway would have minimal impact on the overall NO predictions of the flames presented in this study as the conditions are outside of the pathway active region, moderate pressures and low temperatures, [24, 25]. Similarly, the fuel-NO and the prompt-NO pathways are not considered in this study due to the lack of N- and C-species in hydrogen.

The paper by Curran [32] gives a good insight on how thermochemical models are usually developed. Models are built either following a hierarchical or global approach. Those built in a hierarchical manner will optimise their model according to different subsets, with the first one being the hydrogen oxidation chemistry, followed by C_1 chemistry (CO, CH_4), and then heavier hydrocarbons (C_{2+}). Pollutant formation (NO_x, soot...) is generally optimised last and is added to the combustion model on top of the other subsets. On the contrary to the hierarchical approach, models built in a global manner have been optimised considering all reactions at play as a whole, and

Table 1: Thermochemical models used in this study.

Ref.	Mech. (version)	Color and symbol	Modelled chemistry	Original version		Hydrogen sub-mechanism					
				Entire chemistry		Entire chemistry		H_2/O_2 chemistry		NO_x chemistry	
				Reactions	Species	Reactions	Species	Reactions	Species	Reactions	Species
[49]	**BUT**	— +	H_2, C_1-C_4, NH_3, NO_x	1089	125	252	33	30	11	222	22
[50, 51]	**CRECK** (2003)	— ▼	H_2, C_1-C_6, NH_3, NO_x	2459	159	222	33	23	11	199	22
[1, 52]	**DTU**	— ★	H_2, C_1-C_2, NH_3, NO_x	1397	151	211	33	27	13	184	21
[53]	**ELTE**	— *	H_2	30	12	30	12	30	12	/	/
[54, 55]	**GDF** (3.0)	— *	H_2, C_1-C_6, NH_3, NO_x	934	123	123	22	21	10	102	12
[56]	**GRI** (3.0)	— ●	C_1-C_3, NO_x	325	53	70	19	29	11	41	8
[57]	**KON**	— ♦	H_2	75	15	75	15	75	15	/	/
[58]	**NUIG** (1.1)	— ▲	H_2, C_1-C_{10}, NH_3, NO_x	5966	923	236	34	37	12	199	12
[59]	**SD** (2016-12+2018-07)	— ■	C_1-C_4, NO_x	311	68	64	21	23	11	41	10
[60]	**TUM**	— ×	H_2	19	11	19	11	19	11	/	/
[61]	**XJTUNO**	— ·	H_2, NH_3, NO_x	266	44	243	37	35	12	208	15

have adjusted their reaction rates on data containing any part of the combustion subsets.

Regardless of the construction approach chosen by the models, the optimisation process can be performed following various strategies. One commonly use is to adjust the kinetic rates of the reactions “by hand", as detailed by Curran [32]. In this approach, each reaction is adjusted individually to fit a validation target. This is conducted using direct and indirect measurements. Direct measurements are where kinetic rates are measured directly: *ab initio*, shock tubes, flow reactors. Indirect measurements derive kinetic rates by fitting velocity, species concentrations, and ignition delay data, generally obtained experimentally in flow or jet-stirred reactors, or in burners. To remove the potential for human error introduced during manual adjustment, formal optimisation tools have been developed. This first led to the introduction of globally optimised mechanisms with ignition delay times, flame speeds, speciations, etc. used as targets [56]. More robust approaches have since been used to perform optimisation under uncertainty (statistical, Bayesian inference, etc.) [53, 63, 64], where, not only the nominal measurements (direct and indirect), but also the measurement uncertainty is used to optimise the mechanisms and, in some cases, provide confidence intervals on the predictions.

Despite this understanding, it still remains unclear how most models are optimised. Some models are developed using other models as a base, that they will append to and adjust rates based on new experimental dataset, such as BUT [49]. It therefore renders their categorisation very complex. In this study, the authors have attempted to classify, to the best of their understanding, the 11 thermochemical models into the aforementioned categories.

Only two mechanisms used in this study follow a global optimisation approach, rather than a hierarchical one:

- GRI [56] is a small mechanism, containing few species and reactions, and has been developed to model natural gas combustion with NO_x formation. This mechanism is widely used in the community due to its limited numerical processing time. It is one of the first examples of mathematical optimisation.

- GDF [54, 55] mechanism was also developed to model natural gas combustion and its NO_x formation. In contrast to GRI, it possess many more reactions and species, and the model kinetic rates have been adjusted by hand.

Many mechanisms, and most in this study, base their modelling on a hierarchical approach. They all have optimised the H_2/O_2 core chemistry individually:

- ELTE [53] and TUM [60], use a formal algorithm-based approach to optimise their model. They use uncertainty quantification and probabilistic techniques to adjust the kinetic rates of the H_2/O_2 system. These two mechanisms do not possess a NO_x chemistry, nor any other combustion-chemistry subset, and have been solely developed to model hydrogen combustion.

- BUT [49], CRECK [50, 51], DTU [1, 52], KON [57], NUIG [58], XJTUNO [61], employ the “by hand" optimisation process as described by Curran [32]. Most of them use a similar core chemistry in which the rates of the reactions vary from model to model based on their individual validation targets. NUIG and CRECK are generally recognised as the most comprehensive mechanisms as they include the combustion modelling of many fuels (light to heavy) and for many combustion conditions. BUT and DTU have been developed to model small-chain hydrocarbon combustion, with a detailed core chemistry, and the modelling of a NO_x chemistry. XJTUNO was developed to model $H_2/CO/NO_x$ with no other combustion-chemistry subset. Finally, KON has been developed for the single modelling of hydrogen combustion and does not possess a NO_x chemistry.

It is unclear to the authors how SD [59] has been optimised as no publications accompany the mechanism; however, it is likely that the latter has been optimised using a hierarchical “by hand" method. It is important to note that this NO_x-containing mechanism has been released without any flame-front NO reactions such as for the NNH or the prompt-NO pathway.

Although this classification may not fully describe the model optimisation process, it is important to understand that the specifics of these optimisation processes are still relatively opaque in most instances.

3. Results

Velocity, temperature, and NO concentration measurements are presented in the following subsections for all nine flames. Each experimental profile is extracted at the center-line of the nozzle and is presented as a function of the axial distance between the nozzle ($z \sim 9$ mm) and the stagnation plate ($z = 0$).

3.1. Velocity measurements

Figure 2 presents the measured particle velocity profiles, u_p, obtained for all nine flames. Experimental results are compared to the particle velocity profiles from each thermochemical model considered in this study.

The particle velocity profiles show the expected trend in the stagnation flow configuration: the flow exits the nozzle at $z \sim 9$ mm and the decelerates towards the flame-front ($z \sim 6$ mm) reaching the reference flame speed ($S_{u,ref}$), measured at the velocity minimum, it accelerates through the flame-front, and finally decelerates as it impinges on the plate ($z = 0$). Overall, the technique leads to profiles of high spatial resolution and low uncertainty on the reference flame speed ($\pm$ 2-10%). Equipment limitations lead to a few absent data points in the high-velocity gradient of the flame-front for the flame at $T_{ad} = 2300$ K; however, this does not limit the analysis or the extraction of the boundary conditions in the low-velocity, unburnt region.

All thermochemical models reproduce the general behaviour of the particle motion in the flow field. Despite this, significant discrepancies between the measured and simulated profiles can

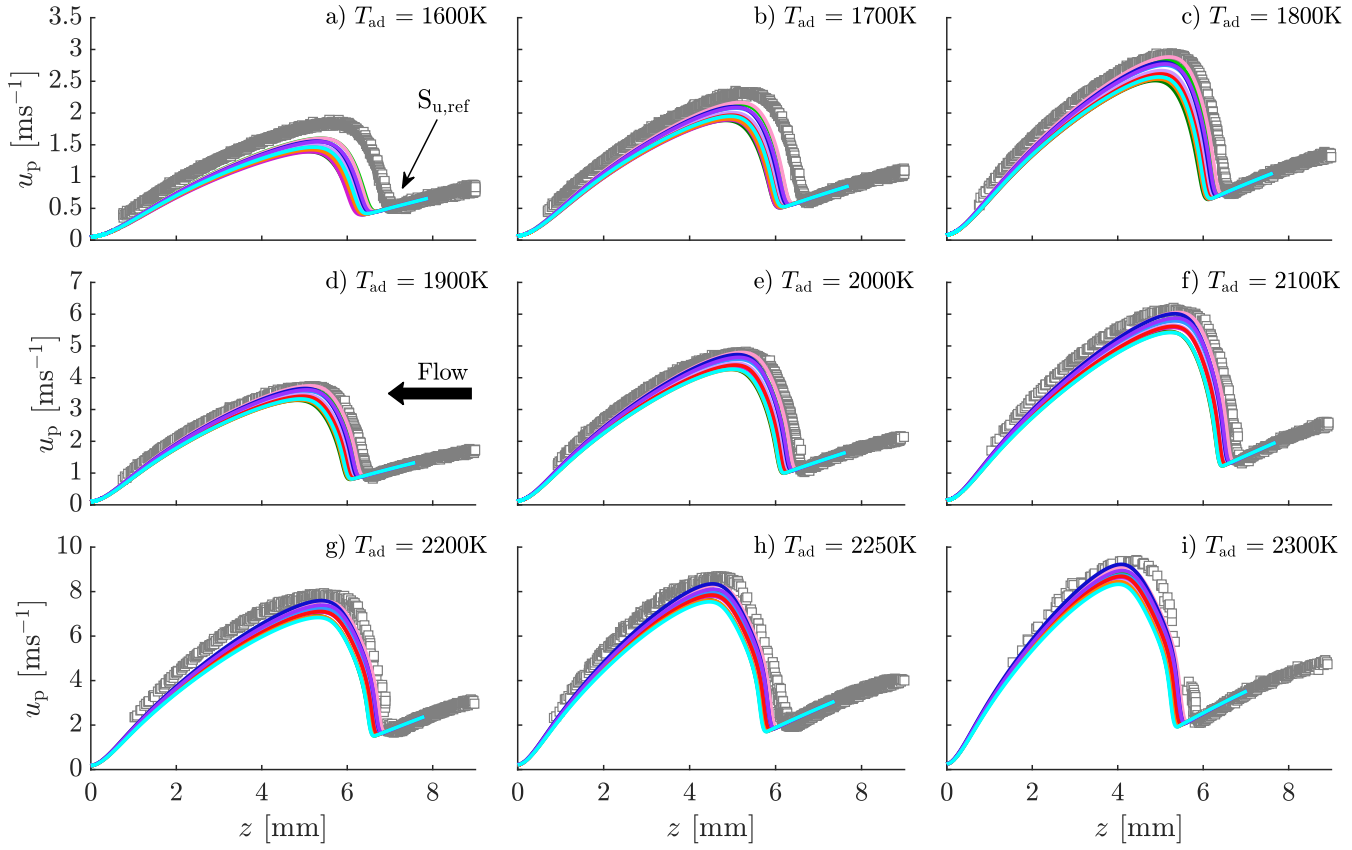

Figure 2: Particle velocity profiles, measured (▫) and simulated (—) using different thermochemical models. The legend follows thecolour-scale presented in Tab. 1. Note the different scale of the velocity profiles between the top, middle, and bottom rows. Note the same velocity scale for a single row of 3 sub-figures.

be observed in the flame position (z_f) defined by the axial location of $S_{u,ref}$.

$S_{u,ref}$ is measured for each flame condition and is presented in Fig. 3a. The ratio of the experimental to the numerical $S_{u,ref}$ is also calculated to determine the level of disagreement between the models and the experiments. Results are presented in Fig. 3b, where a perfect agreement is defined by a ratio of unity. Uncertainties are reported using the shaded area and account for the experimental uncertainty as well as for the uncertainty of the experimentally-measured boundary conditions propagated through the simulations. Discrepancies between the measurements and the simulations outside the shaded region should then arise from model inaccuracies. The calculation methodology of the uncertainties is given in the Supplementary Materials Section 4.

As expected, the reference flame speed increases with the adiabatic flame temperature, as dictated by flame theory. While this general trend is correctly captured by the models, disagreements between the experimental and numerical $S_{u,ref}$ are apparent, particularly at low temperatures, where models unanimously underpredict the reference flame speed by 10% to 20%. Furthermore, the non-linearity of $S_{u,ref,num}/S_{u,ref,exp}$ indicates that the dependence of the thermochemical models with temperature and/or with argon concentration is not correctly predicted. Overall, GDF is the model that performs the best, relative to the

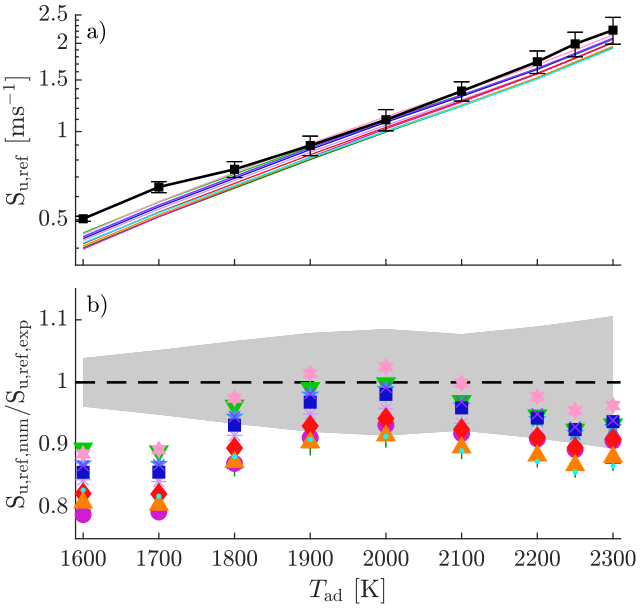

Figure 3: Comparison of the experimental (black) and numerical (colored) of: a) the absolute reference flame speed $S_{u,ref}$, and b) the ratio of the numerical to experimental reference flame speed $S_{u,ref,num}/S_{u,ref,exp}$. Shaded area represent the uncertainties. The legend follows the colour-scale presented in Tab. 1. Note the logarithmic scale used in sub-figure a.

measurements, across the entire temperature range.

These results are consistent with the findings of Durocher et al. [31] who found that mechanisms tend to underestimate the reference flame speed in lean-to-rich, atmospheric, low-temperature, hydrogen-argon-air stagnation flames. These discrepancies lead to the observed disagreement in the flame position. With a lower predicted flame speed, the numerical flame stabilises in the region of lower flow velocity, further away from the nozzle.

Such disagreements in the velocity profiles prove the presence of inaccuracies in the base chemistry driving hydrogen oxidation, especially at the low- and high-end temperatures. Further investigation is performed in this study (see Section 4 to 7) to identify the origin of the disagreement.

3.2. Temperature measurements

The measured and simulated temperature profiles are presented in Fig. 4. The temperature of the flow remains at ambient conditions in the unburnt region, it then sharply increases in the flame-front, follows a more gentle increase in the post-flame region, and then, finally, decreases as it reaches the stagnation plate. All thermochemical models capture the profiles accurately, for all conditions tested, within experimental uncertainty. This is expected as the thermodynamic parameters of the species involved in these flames are well known. Only a discrepancy in the flame position can be observed on the profiles, as discussed for the velocity profiles. Finally, these temperature profiles confirm that the target adiabatic flame temperature is reached by each flame.

3.3. NO concentration measurements

Figure 5 displays the NO-LIF signal profiles obtained experimentally and numerically for all conditions. Estimates of the NO concentration in ppm is given on the right-hand vertical axis of each graph. This estimation is valid in the post-flame region only, except within the plate thermal boundary layer ($z \lesssim 1.0$ mm). Further details of the calculation is given in the Supplementary Materials Section 3. The profiles presented are the result of an average of profiles measured twice for each condition.

The measured NO-LIF profiles follow the expected trend: an absence of signal in the unburnt region followed by a sharp increase through the flame, defining the flame-front ($z \sim 6$ mm), and a transient increase in the post-flame region ($z \sim 5.5$ mm to $z \sim 1$ mm). Note that the NO-LIF signal increases as it approaches the stagnation plate due to the thermal effect of the cold boundary layer, increasing the NO number density even at constant NO mole fraction. For a given axial position throughout all nine flames, the signal increases with the increase of the

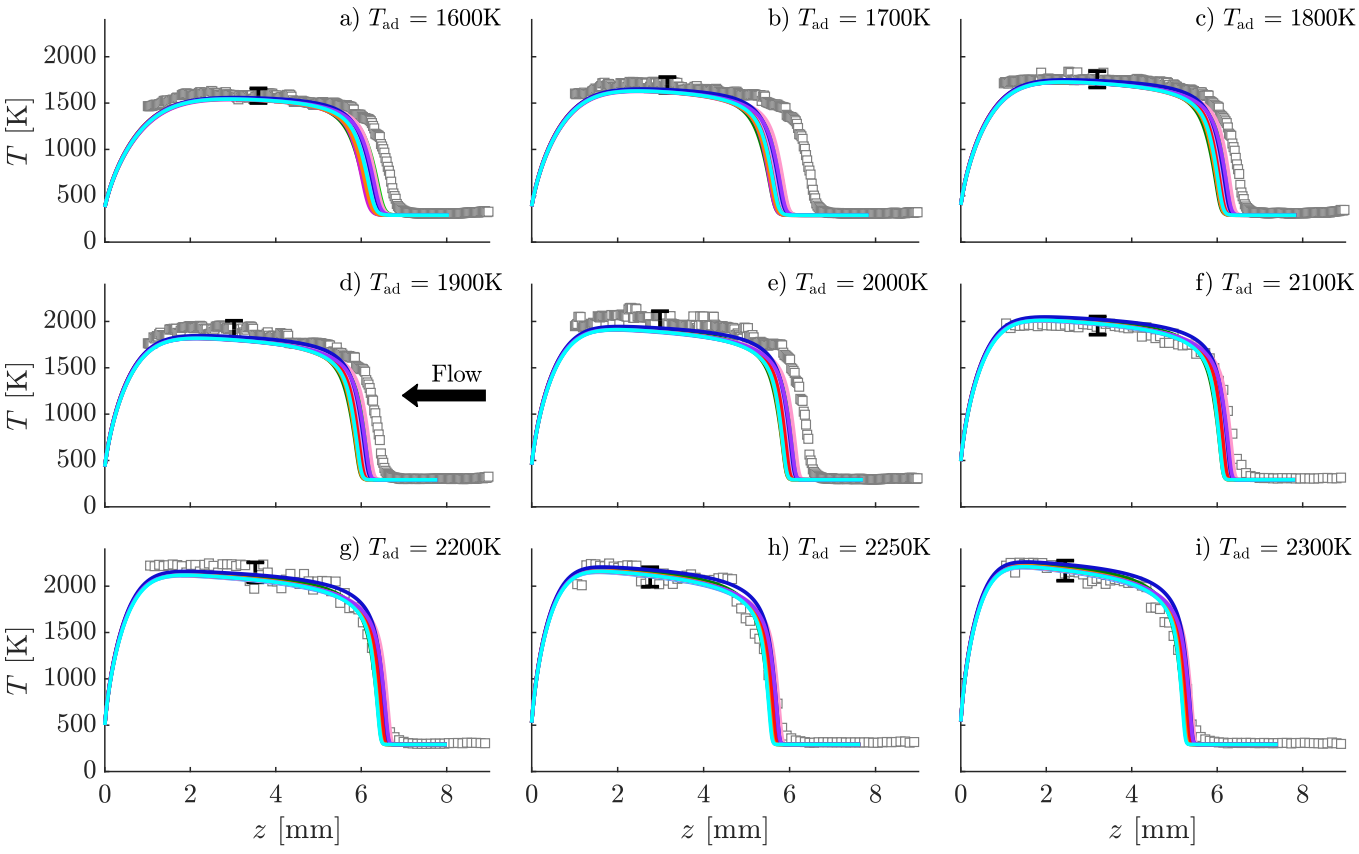

Figure 4: Temperature profiles, measured (▫) and simulated (—) using different thermochemical models. The legend follows the colour-scale presented in Tab. 1. The signal close to the stagnation plate, at z <1 mm, is not plotted due to a low signal-to-noise ratio. Note the same temperature scale for a single row of 3 sub-figures.

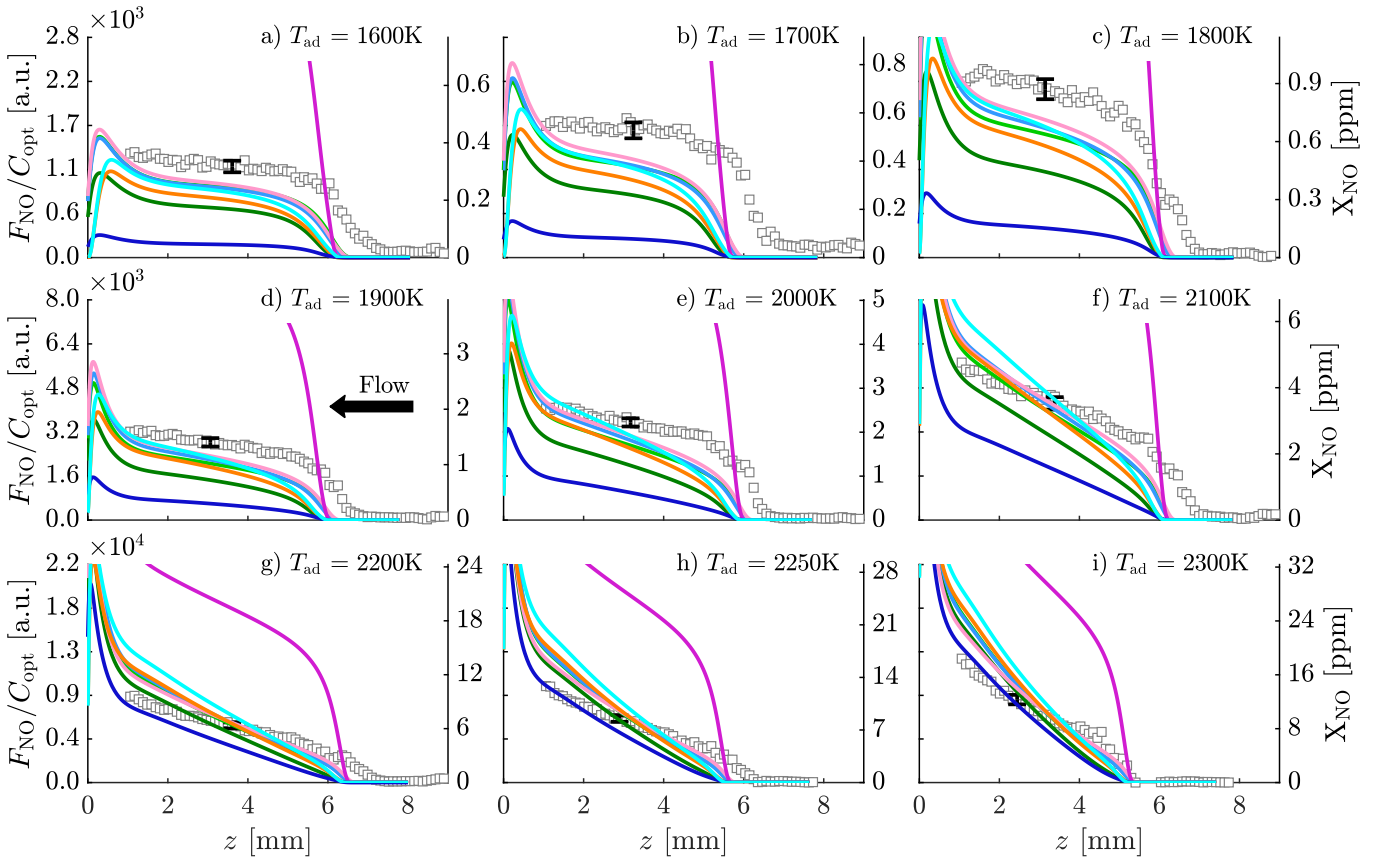

Figure 5: NO-LIF signal profiles, measured (▫) and simulated (—) using different thermochemical models. The legend follows the colour-scale presented in Tab. 1. Note the same NO-LIF signal scale for a single row of 3 sub-figures. Estimates of NO production in ppm is provided on the right-hand vertical axis of each sub-figure. The signal close to the stagnation plate, at z <1 mm, is not plotted due to a low signal-to-noise ratio.

adiabatic flame temperature, as expected from the dependence of the thermal-NO pathway with temperature.

While the measured profiles are of high resolution and relatively low uncertainty ($\sim \pm 6\%$ on average for all flames), no thermochemical models are able to accurately capture the measured profiles. Models tend to underestimate the contribution of the flame-front NO while they overestimate the rate of NO formation in the post-flame region. None of the models appear to precisely capture either the flame-front or the post-flame NO for more than a few axial points, and none are able to capture both regions at the same time. These observations apply to all flames considered in this study.

These discrepancies can be better observed in Fig. 6, where the absolute signals and the ratios are presented for a location in the flame-front, in the post-flame, and for the slope of the profile. Details of the extraction of these parameters from the measured and simulated NO-LIF profiles are given in the Supplementary Materials Section 5. Note that large uncertainties are present at low temperatures due to the very low signal (sub-ppm NO concentrations) at these flame temperatures. Additionally, the extraction of the absolute flame-front NO and the slope of the NO signal in the post-flame region is performed in such a way to be independent from upstream velocity mispredictions. In contrast, the absolute post-flame NO signal is extracted such that it is dependent on any mispredictions upstream to the extraction location.

Figure 6a shows that the measured flame-front NO increases with the increase in the adiabatic temperature, and appears to plateau (note the logarithmic scale used in the figure) at temperatures around 2200 K. Correspondingly, Fig. 6d shows that the simulations generally follow the temperature dependence of the measurement (flat trend) up to 2200 K. However, it is apparent from Fig. 6a and d that large discrepancies are present between the simulation and experimental results, across the entire temperature range, especially at high temperatures. The ratio of the numerical to the experimental absolute flame-front NO signal demonstrates the notable overprediction of GRI stemming from a known overestimation of the NNH pathway in the flame-front region [14], most likely due to the fact that GRI was solely optimised to model natural gas and not hydrogen. Inversely, SD significantly underpredicts the flame-front NO due to the absence of any reaction contributing to flame-front NO formation. All other models also consistently underpredict the flame-front NO signal, especially at high temperatures. Nevertheless, the flat trends of the mechanisms up to ~2100 K, observed in Fig. 6d, indicates that the dependence with temperature of the reaction(s) (through either the activation energy or the temperature coefficient of the Arrhenius equation) involved in the formation of flame-front NO is well described. Therefore, the observed discrepancies are potentially due to an inaccurate

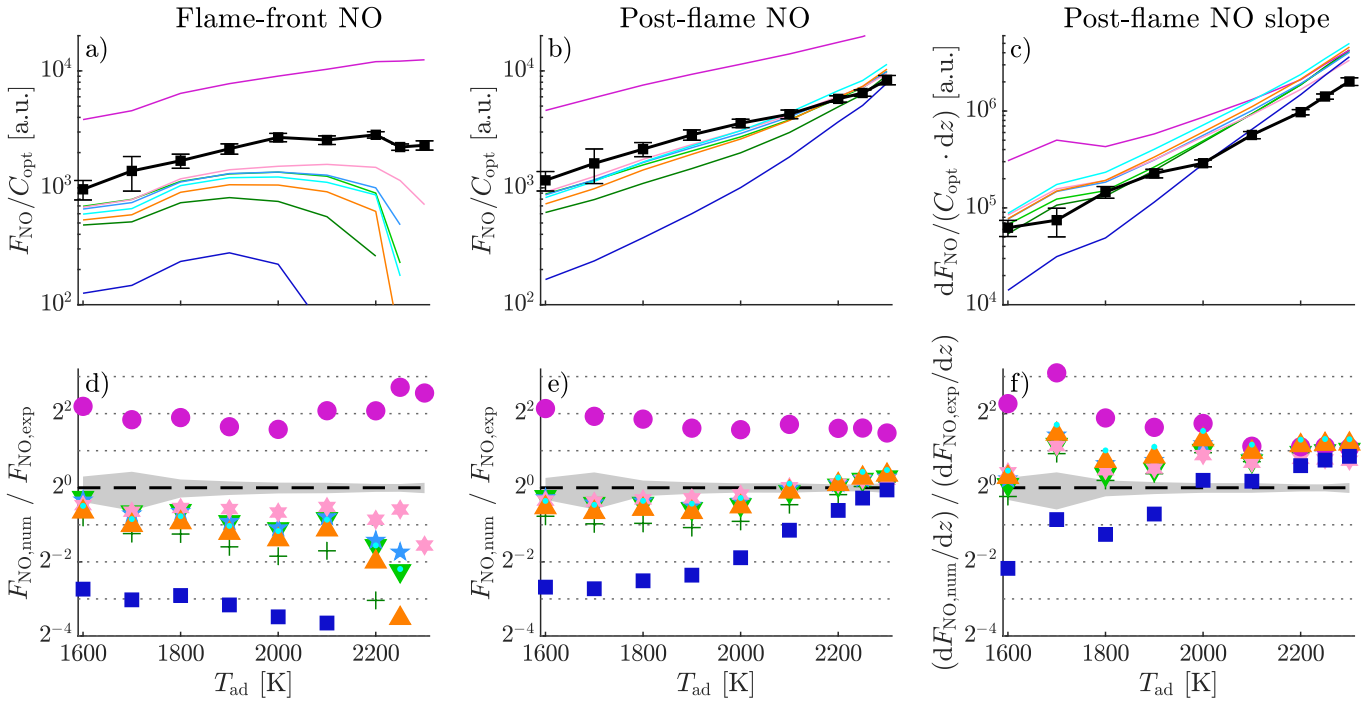

Figure 6: Comparison of experimental (black) and numerical (colored): a) the absolute NO-LIF signal in the flame-front, b) the absolute NO-LIF signal in the post-flame region at z_f-3.5 mm, c) the slope of the post-flame NO-LIF signal, and their respective numerical to experimental ratios (d-f). The legend follows the colour-scale presented in Tab. 1. Shaded areas represent the root-sum square of both the experimental and numerical uncertainties. Note the logarithmic scale used in sub-figures a-c (base 10) and d-f (base 2).

description of the Arrhenius pre-exponential factor of the reaction(s) responsible for NO production in this region.

As indicated in Fig. 6b, the measured NO-LIF signal in the post-flame region increases exponentially (note the logarithmic scale in Fig. 6) with the increase of the adiabatic flame temperature. This behaviour is expected, as the flame-front and post-flame NO are intrinsically linked, such that an increase of the absolute signal in the flame-front region will lead to an increase of the signal in the post-flame region, assuming that NO-reburn does not occur. It is, therefore, expected to find that GRI and SD have similar inaccuracies than what is observed for the flame-front NO. In Fig. 6e, it can be seen that mechanisms all have the same flat trend up to ∼2000 K, underpredicting the measurement (except GRI). Beyond this temperature, there is a shift in the prediction trends, and models tend to overpredict the measurement from ∼2100 K. The trend in the model predictions suggests an inaccurate dependence on temperature of the reactions controlling post-flame NO formation, through either the activation energy or the temperature coefficient.

Finally, it is apparent in Fig. 6c that the spatial rate of change of NO (slope) in the post-flame region is also increasing with temperature. This indicates that some, if not all, of the NO-producing pathways active in the post-flame region are spatially- and temperature- dependent for these flames. Fig. 6f shows the significant disagreements observed between the experiments and the simulations for the post-flame rate of change of the NO-LIF signal. At low temperatures, few models are within uncertainty, while GRI overestimates the value and SD underestimates it. At temperatures above 1900 K, all models unanimously overpredict the rate of change of NO. This trend in predictions proves that there is an overprediction of the spatial and temperature dependence of the reactions controlling post-flame NO. This leads to overpredictions of the rate of formation of NO around 225% for all the models studied at $T_{ad} \geqslant 2200$ K. This discrepancy is much larger than the measured uncertainty (∼6%) for the rate of formation of NO for these conditions with steep slopes.

This discrepancy in NO prediction worsens if the residence time of typical gas turbines is taken into account. Indeed, the residence times of the flames measured in this study vary from ∼2.5 ms at 1600 K to ∼0.5 ms at 2300 K (at the location of the uncertainty calculation), which is much lower than the residence time in traditional hydrocarbon combustion systems.

To explore this effect, Fig. 7 presents an extrapolation of the measured signals of Fig. 5a, e, and f, to longer residence times. A residence time of 10 ms is selected to represent a practical combustion chamber. It is apparent that the models significantly diverge with increasing residence time. Extrapolated model predictions of absolute NO concentration, at 10 ms, vary from -90% to +270% relative to the extrapolated measured profile. This is of significant concern for any practical application when these models are used to identify promising designs within sub-ppm targets.

The findings of this section are consistent with Meulemans et al. [14] who found that no thermochemical models could correctly reproduce the NO-LIF signals measured in methane flames at adiabatic temperatures from 1900 K to 2500 K. They

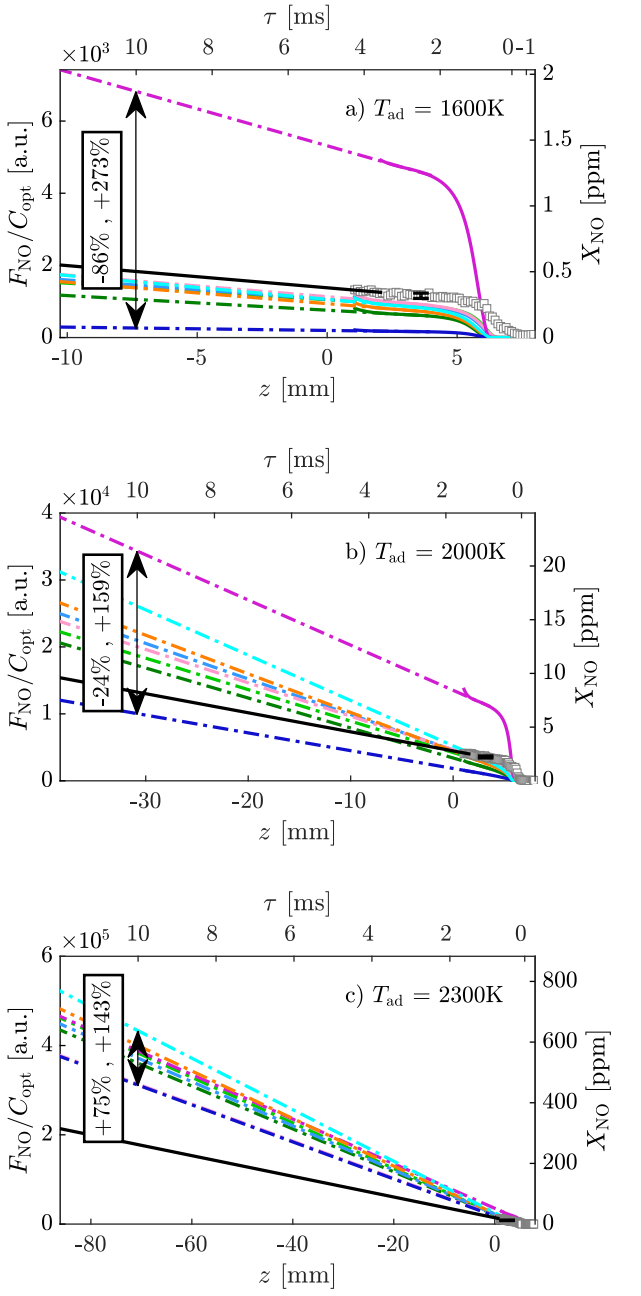

Figure 7: Extrapolated numerical (- -) and experimental (–) profiles of NO-LIF signal results of the flame at T_{ad} = a) 1600 K, b) 2000 K, and c) 2300 K, to 10 ms residence time. Residence time is calculated the experimental velocity profiles. The origin (0 ms) is determined at the location of the reference flame speed, z_f. The legend follows the colour-scale presented in Tab. 1.

attributed the disagreements to an imprecise description of the models' chemistry, principally due to mispredicting the interaction between the four NO-producing pathways, with some minor contribution to the base radical chemistry. They found that the NO_x sub-chemistry NOMecha2.0 (attached to KON v.0.6) was the best in predicting the NO rate of change in the post-flame region across the entire range of temperature. Despite this, in the current study, this specific sub-chemistry (attached to GDF) significantly overpredicts the NO rate of change in the post-flame region at high temperatures. Thus, despite the agreement of NOMecha2.0 for the methane study, the contributions of the change in fuel has changed its prediction behaviour relative to measurements. This suggests that the base chemistry may have a larger contribution to NO slope misprediction than previously hypothesised.

It is worth noting that the optimisation method used by the models, hierarchical or global, and mathematical or "by hand", does not appear to have an impact on the accuracy of the model predictions, either for the velocity or NO concentration measurements.

4. Sensitivity analysis

A sensitivity analysis is performed using the GDF mechanism to identify the reactions that have the greatest influence on flame speed and NO concentrations. This mechanism is used as a reference in this study because it shows the closest agreement with the velocity and NO-LIF measurements.

A brute-force method is used by applying a perturbation of 1% sequentially on the reaction rate constants of the reference mechanism. Duplicate reactions are only perturbed once by applying the perturbation on all duplicates simultaneously, resulting in only one sensitivity value for the set. The 15 most sensitive reactions to four chosen parameters are extracted in order of importance following the decreasing value of the root sum square of the four Logarithmic Sensitivity (L.S.) for each reaction (R_i). The four parameters are: $S_{u,ref}$, the absolute flame-front NO, and the post-flame NO absolute concentration and slope. While all reactions are reversible, the reaction labels display the directionality determined using the net rate of progress of the reactions, for example R_I : NNH + O → NH + NO has a net production of NH and NO species. Logarithmic sensitivities are obtained by normalizing the solution by the perturbation, such that a L.S. presents a relative change in the quantity of interest with respect to the change in the reaction rate constant. A positive sensitivity on a reaction indicates that an increase of its rate would lead to an increase of this parameter value, *e.g.* $\text{L.S.}(R_I)|_{X_{NO,PF}} = 0.5$ implies that an increase of the reaction rate of R_I of 1% would lead to an increase of the post-flame NO concentration by 0.5%. Therefore, results of the sensitivity analysis can be directly compared to the discrepancies observed between the measurements and the models in Fig. 3 and Fig. 6.

Figure 8 presents the results of the analysis performed on all nine flames, for the four parameters cited previously.

4.1. Reference flame speed

Unsurprisingly, the reference flame speed is not sensitive to any of the NO forming reactions. Instead, $S_{u,ref}$ is highly sensitive to the hydrogen oxidation elementary reactions [65], namely the hydrogen-oxygen shuffle reactions:

$$H_2 + OH \rightarrow H + H_2O \quad (R_{II})$$
$$H + O_2 \rightarrow O + OH \quad (R_{III})$$
$$H_2 + O \rightarrow H + OH \quad (R_{XI})$$

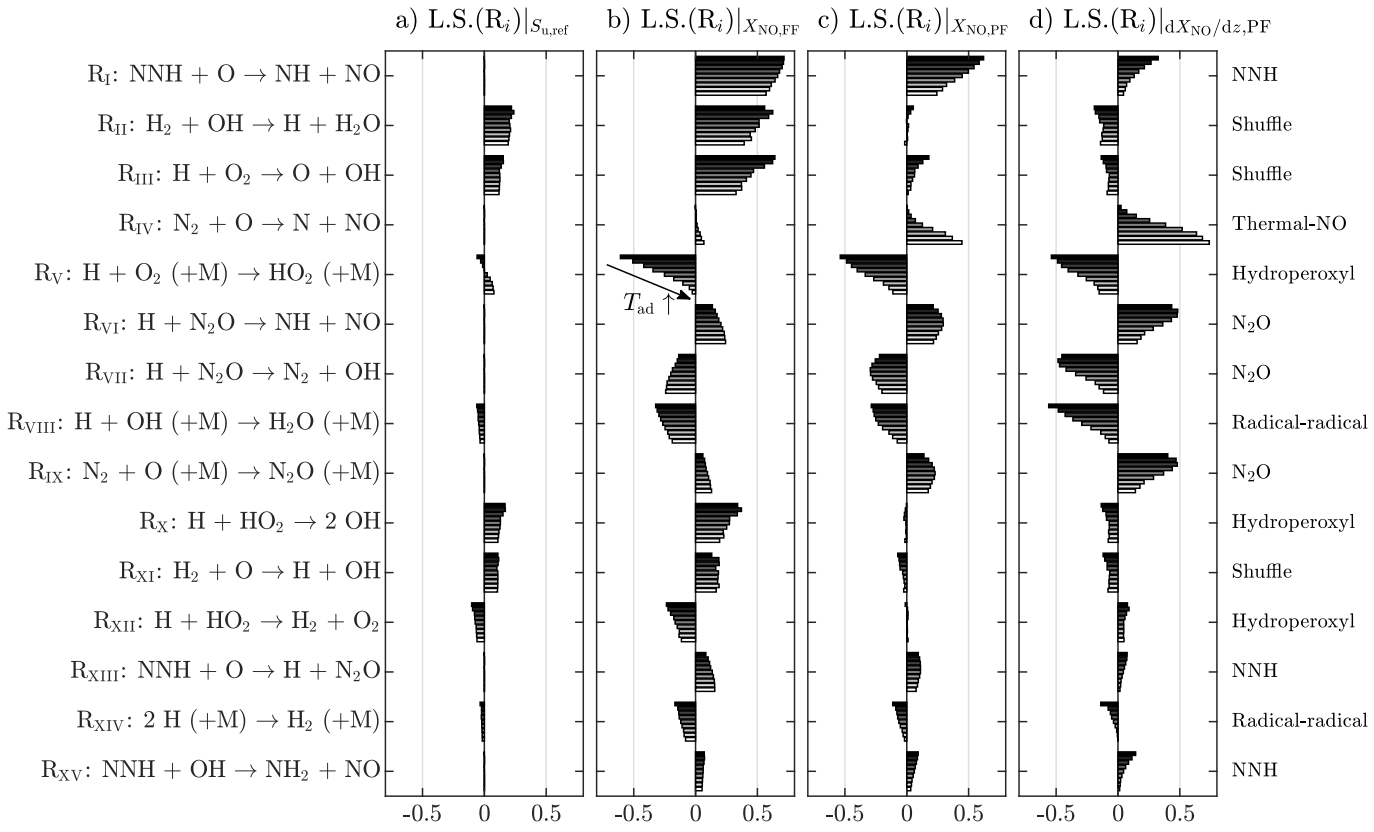

Figure 8: Brute-force sensitivity analysis performed using GDF on four parameters: a) the reference flame speed $S_{u,ref}$, b) the concentration of NO in the flame-front $X_{NO,FF}$ c) the concentration of NO in the post-flame $X_{NO,PF}$ at z_f-3.5 mm, and d) the NO rate of change dX_{NO}/dz. Results for the nine flame conditions are presented using a gradient in grey from T_{ad} = 1600 K (black) to T_{ad} = 2300 K (white).

the hydroperoxyl reactions:

$$H + O_2\ (+M) \rightarrow HO_2\ (+M) \qquad (R_V)$$
$$H + HO_2 \rightarrow 2OH \qquad (R_X)$$
$$H + HO_2 \rightarrow H_2 + O_2 \qquad (R_{XII})$$

and the radical-radical recombination reactions:

$$H + OH\ (+M) \rightarrow H_2O\ (+M) \qquad (R_{VIII})$$
$$2H\ (+M) \rightarrow H_2\ (+M) \qquad (R_{XIV})$$

These three groups of hydrogen oxidation elementary reactions fully control the radical pool present in the flame with the hydrogen-oxygen shuffle reactions producing the radicals H, O, and OH; the hydroperoxyl reactions, producing and consuming HO_2 through radicals; and the radical-radical recombination reactions rearranging the radical pool through recombination. These reactions govern the combustion taking place in all hydrogen-containing fuels.

In this study, only 8 reactions control the radical pool of these flames, however, changing the rate of a single one of them would not allow the solving of $S_{u,ref}$ mispredictions observed in Fig. 3, as the trend of sensitivity with temperature of each of the 8 reactions does not match the trend of discrepancy with temperature of $S_{u,ref}$. Reactions with a positive sensitivity (R_{II}, R_{III}, and R_X) seem to have a higher sensitivity at low temperatures, where the observed discrepancies between the measurements and simulations are most significant. It is also interesting to note the temperature dependence of the sensitivity of R_V, with a negative L.S. at low temperatures, an almost zero L.S. at moderate temperatures, and a positive L.S. at high temperatures. Therefore, R_V could potentially help in balancing the high sensitivity at the low-end temperatures of the other reactions (R_{II}, R_{III}, and R_X) in order to improve the flame speed predictions.

As discussed, it is clear that resolving the flame speed mispredictions in Fig. 3 requires resolving the complex behaviour of several reactions and their interactions. As shown by the sensitivity analysis, the balance of the 3 groups of reactions, and their impact on the radical pool, is of significant importance in attempting to close the velocity prediction gap at low- and high-end temperatures. Designing more experiments targeting these regions specifically could produce better model improvement by challenging the established kinetic models with datasets outside the typical validation ranges.

4.2. Flame-front NO

It is expected to find that flame-front NO is highly sensitive to not only NO-formation reactions, but also to some hydrogen oxidation reactions governing the radical pool. For hydro-

gen flames, flame-front NO is dominantly sensitive to the NNH pathway:

$$NNH + O \rightarrow NH + NO \quad (R_I)$$
$$NNH + O \rightarrow H + N_2O \quad (R_{XIII})$$
$$NNH + OH \rightarrow NH_2 + NO \quad (R_{XV})$$

and, less significantly, to the N_2O pathway:

$$H + N_2O \rightarrow NH + NO \quad (R_{VI})$$
$$H + N_2O \rightarrow N_2 + OH \quad (R_{VII})$$
$$N_2 + O\ (+M) \rightarrow N_2O\ (+M) \quad (R_{IX})$$

These two pathways are highly dependent on the formation of H, O, and OH radicals through the base chemistry. Therefore, NO formation in the flame-front is favored if these radicals are favored (through R_{II}, R_{III}, R_X, and R_{XI}), and disfavored through the consumption of these radicals (R_V, R_{VIII}, R_{XII}, and R_{XIV}).

Furthermore, it is observed in the NO measurements that the temperature dependency of the reactions appears to be accurately captured by GDF up to 2100 K (Fig. 6d), despite this model consistently underpredicting the measurement. Changing the reaction rate of the hydrogen oxidation reactions to improve $S_{u,ref}$ would potentially be sufficient to also improve the prediction of the flame-front NO, without having to change the NO-formation reaction rates. Increasing the rates of R_{II}, R_{III}, R_X, and R_{XI} would increase the predictions in $S_{u,ref}$ and in $X_{NO,FF}$ across the entire range of temperature and, therefore, reduce the gap of predictions between GDF and the measurements observed in Fig. 3b and Fig. 6d. As a matter of fact, only changing the rate of the NO-formation reactions would not be sufficient to improve the prediction of flame-front NO. It would therefore be ill-advised to optimise the NO_x sub-chemistry without considering changes in the base chemistry, as well. These results indicate that the optimisation of the base chemistry of any combustion model could be performed using, not only the velocity results ($S_{u,ref}$), but also using NO concentration measurements in the flame-front ($X_{NO,FF}$) as they are strongly dependent on the hydrogen oxidation reactions.

4.3. Absolute post-flame NO

In contrast to the sensitivity analysis performed on the flame-front NO, the sensitivity analysis performed on NO at a given location of the post-flame region (3.5 mm from the reference flame speed z_f) could be influenced by either the flame-front or post-flame formation mechanisms. Depending on how far the analysis is performed from z_f, the results will be more or less dependent on the flame-front chemistry. Therefore, the sensitivity analysis performed on the spatial rate of change of NO in the post-flame region is more relevant in this study to understand the role played by the reactions in this region.

Despite this, $L.S.(R_i)|_{X_{NO,PF}}$ shows in Fig. 8c that, if a model was to be optimised on a sensitivity analysis performed at one given location, disregarding any spatial information, this could lead to an inaccurate model. If one was to refer to $L.S.(R_i)|_{X_{NO,PF}}$ uniquely, the contribution of many reactions playing an important role otherwise in $L.S.(R_i)|_{X_{NO,FF}}$, for example through R_{II}, could be underestimated, or disregarded, in the optimisation process.

4.4. Rate of change of post-flame NO

The spatial rate of change of NO in the post-flame region is, unsurprisingly, highly dependent on the thermal-NO initiation reaction:

$$N_2 + O \rightarrow N + NO, \quad (R_{IV})$$

especially at high temperatures. In fact, as the adiabatic temperature is increased and, consequently, the thermal pathway sensitivity is increased, the sensitivity of the NNH and N_2O pathways is decreased. This is not due to a change of reactivity of the NNH and N_2O reactions with increased temperature, but rather due to the channeling of the O-atoms through the thermal pathway, reducing their availability in the radical pool for R_I and R_{IX}. This suggests that the three NO-forming pathways have a spatial inter-dependency, likely due to the radical pool depletion. This behaviour is considerably different than the behaviour observed in hydrocarbon flames. The strong spatial dependency of the N_2O and NNH pathways, in the post-flame region of hydrogen flames, is almost non-existent in the previous methane flames study [14]. Indeed, in the post-flame region of hydrocarbon flames, the radical pool, especially for H atoms, is less present and is mostly depleted through the flame-front as it is required to breakdown the fuel bond. A comparison of such flames is presented in the Supplementary Materials Section 7.2 to support this hypothesis. As a result, it is possible that the more significant impact of the radical dependence of NO-formation pathways in hydrogen flames are overlooked due to their relatively weaker effect in hydrocarbon flames.

Interestingly, despite the sensitivity of dX_{NO}/dz to the N_2O pathway, the latter is likely not responsible for any NO formation through R_{VI}. This is because the reaction forming N_2O from N_2 (R_{IX}) is almost entirely balanced by the reaction forming N_2 from N_2O (R_{VII}).

Furthermore, the overall negative sensitivity of the hydrogen oxidation reactions indicates that any change in the radical pool, especially the consumption of radicals, would decrease the post-flame NO rate of change, especially at low temperatures through R_V and R_{VIII}.

This, once again, suggests that the base chemistry is one of the biggest drivers in improving the predictions of NO measurements. Nevertheless, in this instance, the change of the reaction rate of the hydrogen oxidation chemistry would not solely suffice to resolve the mispredictions of GDF regarding the NO rate of change in the post-flame region. Indeed, all the base chemistry reactions have a negative sensitivity, stronger at low-end than at high-end temperatures. This would have implied that GDF would be less accurate at low-end temperatures and yet, the opposing trend is shown in Fig. 6f. Therefore, the adjustment of some NO-formation reactions seems inevitable to compensate for the optimisation of the hydrogen oxidation reactions to target $S_{u,ref}$ and $X_{NO,FF}$.

It is clear that a complex combination of reaction rate inaccuracies interact in this study. The three NO-formation pathways are highly dependent on O, H, and OH radical formation. The three pathways are also highly dependent on each other through the competition for these radicals. Therefore, any imbalance in the prediction of the reaction rate of any elementary reaction could lead to significant discrepancy in the prediction of NO formation through any of the three NO-forming pathways in hydrogen flames. This analysis demonstrates that optimisation efforts have to be conducted targeting several spatially-dependent parameters in order to account for all reactions playing a role in the hydrogen combustion-chemistry.

Finally, this analysis introduces NO data as a potentially additional parameter that can be used when optimising and validating the velocity prediction performance of a thermochemical model, and its associated base chemistry. As observed in Fig. 8, the sensitivity on the hydrogen oxidation reactions is stronger for $X_{\mathrm{NO,FF}}$ than for $S_{\mathrm{u,ref}}$. This would allow improved constraints on the optimisation of the base chemistry reactions, especially in cases where velocity measurements are uncertain and less sensitive than NO measurements [66].

5. Reaction kinetic rates

5.1. Hydrogen oxidation chemistry

Despite the relatively simple chemistry involved in the oxidation process of hydrogen, many reactions still possess large uncertainties [57, 65, 67–69].

Figure 9 presents the reaction rates of all mechanisms used in this study for the 8 hydrogen oxidation reactions identified as the most important reactions presented in the sensitivity analysis. The reaction rates are plotted in the direction that corresponds to a positive net rate of progress, and are extracted using Cantera, such that, if a reaction is only specified in the reverse direction, the forward rate is the same as what would be used within the simulations, with the calculation using the equilibrium constant.

The discrepancy in the reaction rate given by the different mechanisms, $\Delta \log_{10}(k_i)$, is calculated as the average of the span, $(\log_{10}(k_i)|_{\max} - \log_{10}(k_i)|_{\min})/2$, at each temperature between 400 K and 2300 K. It is important to note that this measurement is not representative of the current uncertainty bands of a reaction. Instead, $\Delta \log_{10}(k_i)$ is only indicative of the similarity between the models for a given reaction rate. Therefore, a low $\Delta \log_{10}(k_i)$ could imply that the reaction has been studied extensively and the uncertainty bands are tight and constrained, but it could also mean that this reaction has, conversely, not been studied as much, and mechanisms use a common rate due to the lack of measurements and studies on this reaction. When available, the reliability of the preferred reaction rate given by Baulch et al. [67] is displayed as $\Delta \log_{10}(k_i)_{\mathrm{B}}$. This gives an insight of the amount of experimental work used to bound the reaction rate, as these preferred rates are still widely used by the models. Therefore, a tight $\Delta \log_{10}(k_i)$ with a larger $\Delta \log_{10}(k_i)_{\mathrm{B}}$ is indicative of a lack of data on this reaction, at least up until 2005.

Defining $\Delta \log_{10}(k_i) < 0.2$ as being a strong similarity between the models for R_i, several of the base reactions possess a tight agreement:

$$\mathrm{H_2 + OH \rightarrow H + H_2O} \quad (\mathrm{R_{II}})$$
$$\mathrm{H + O_2 \rightarrow O + OH} \quad (\mathrm{R_{III}})$$
$$\mathrm{H + O_2\ (+M) \rightarrow HO_2\ (+M)} \quad (\mathrm{R_V})$$
$$\mathrm{H + HO_2 \rightarrow 2OH} \quad (\mathrm{R_X})$$
$$\mathrm{2H\ (+M) \rightarrow H_2\ (+M)} \quad (\mathrm{R_{XIV}})$$

These reactions all have a similar temperature dependence, but vary slightly in the activation energy of their Arrhenius equations. Despite the strong similarity between the models, some of these reactions were identified to contain large uncertainty in their rates [69, 70]. $\mathrm{R_{III}}$ and $\mathrm{R_V}$ are some of the most important reactions due to their role in determining the 2$^{\mathrm{nd}}$ explosion limit in H_2/O_2 systems. Despite many studies dedicated to the measurement of their reaction rates, an uncertainty of up to 20% is still expected in flame speed [57, 68], due to the current understanding of the collisional energy transfer properties involved in $\mathrm{R_V}$. This impacts $\mathrm{R_{III}}$ through the competition for H atoms. In this study, the agreement observed between the models actually hides the large uncertainty linked to these reaction rates, and likely points to mechanisms simply assuming the same reaction rate and focusing on other reactions during their optimisation processes. In contrast,

$$\mathrm{H + OH\ (+M) \rightarrow H_2O\ (+M)} \quad (\mathrm{R_{VIII}})$$
$$\mathrm{H_2 + O \rightarrow H + OH} \quad (\mathrm{R_{XI}})$$
$$\mathrm{H + HO_2 \rightarrow H_2 + O_2} \quad (\mathrm{R_{XII}})$$

display a relatively large spread in their rates ($\Delta \log_{10}(k_i) > 0.3$). For $\mathrm{R_{VIII}}$, it appears that the discrepancy arises from a difference in the activation energies. It was also identified by Burke et al. [68] to not be able to accurately describe the flame behaviour over a wide range of pressures and temperatures, due to the high dependency of the bath gas description. In this study, $\mathrm{R_{VIII}}$ is active in both the flame-front and the post-flame region and is responsible for depleting the H and OH radical pool available throughout the domain. Disagreements in the rate of the models lead to differences in the concentration of these radicals and, therefore, would lead to differences in the concentration of NO, in both the flame-front and the post-flame region, as observed in the sensitivity analysis.

$\mathrm{R_{XI}}$ and $\mathrm{R_{XII}}$ display significant disagreement in the temperature dependency of their rates. It was shown by Burke et al. [68] that $\mathrm{R_{XII}}$ (along with $\mathrm{R_X}$), participate in the 2$^{\mathrm{nd}}$ explosion limit and is not well known at high temperatures. In this study, Fig. 8 shows that $\mathrm{R_{XI}}$ and $\mathrm{R_{XII}}$ are mostly active in the flame-front, and are responsible for the consumption and recombination of H_2 through the use of O and H atoms. Disagreements in the rates of these reactions throughout the models would lead to disagreements in the concentration of NO formed through the flame-front, as well as disagreements in the reference flame speed.

As discussed, these 3 reactions, $\mathrm{R_{VIII}}$, $\mathrm{R_{XI}}$, and $\mathrm{R_{XII}}$, ap-

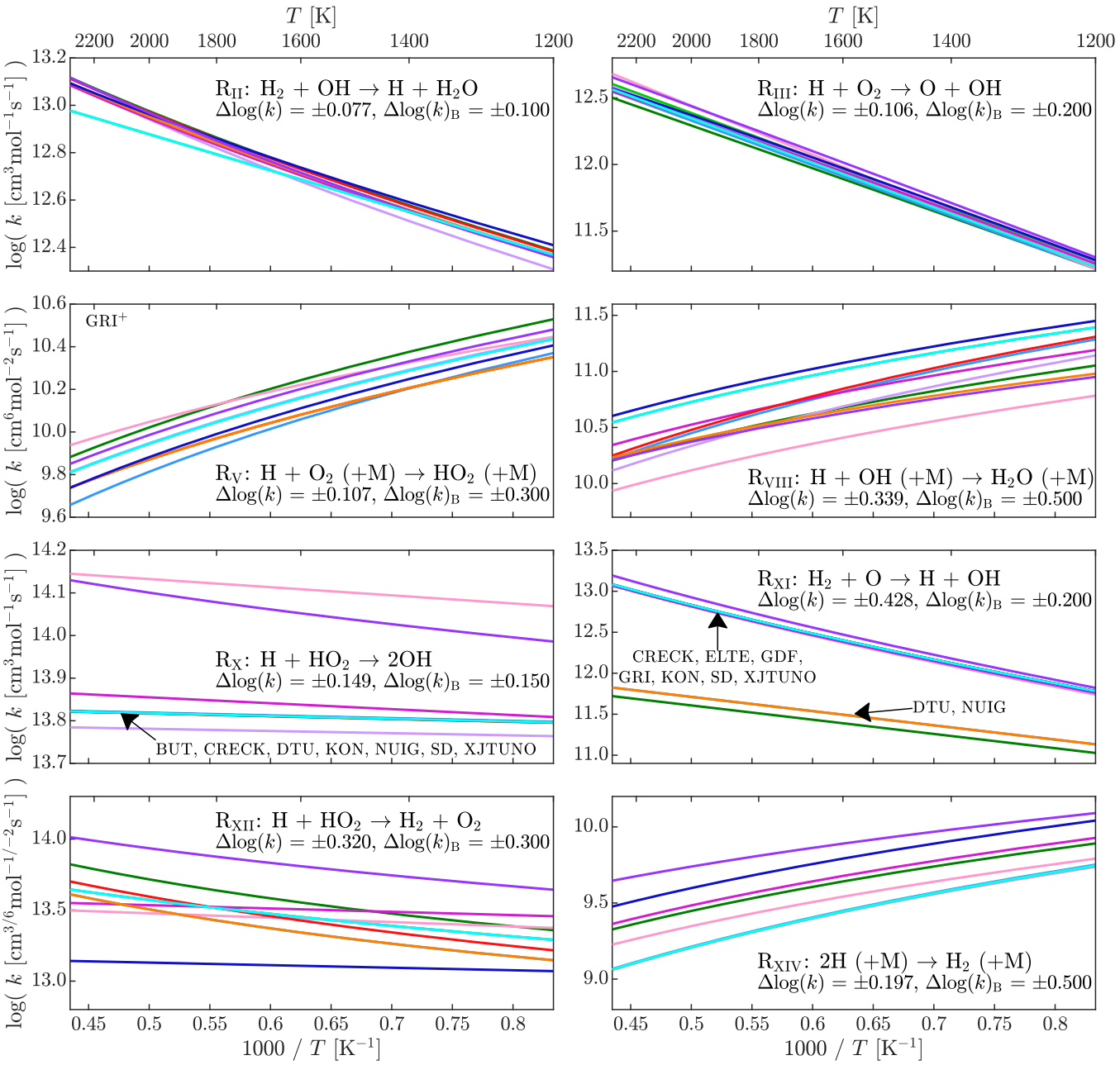

Figure 9: Arrhenius plot of the 8 base chemistry reactions identified in the sensitivity analysis. The rate is presented according to the directionality of the reaction determined using the net rate of progress of the reactions. Rates are extracted for each mechanism using Cantera at temperatures from 400 K to 2300 K. The spread of the reaction rate within this temperature range is represented by $\Delta \log_{10}(k_i)$. The legend follows the colour-scale presented in Tab. 1.Please note the difference of units between bimolecular [$cm^3.mol^{-1}.s^{-1}$] and termolecular [$cm^6.mol^{-2}.s^{-1}$] reaction rates. GRI$^+$: this model indicates a collision factor of 0 for O_2, H_2O, N_2, and Ar for R_V, leading to a null rate for these flames.

pear to be at the origin of the discrepancies between the models in both the velocity and NO concentration predictions of this study. Tightening the uncertainty of these rates would likely contribute to an improved description of the parameters presented in the sensitivity analysis.

5.2. NO_x sub-chemistry

Figure 10 presents the reaction rates of the 7 NO_x reactions identified as the most important reactions presented in the sensitivity analysis. This shows a relatively moderate span of $\Delta \log_{10}(k_i)$ observed for most of the NO-formation reaction rates. The reactions presenting a large span,

$$NNH + O \rightarrow NH + NO \quad (R_I)$$
$$H + N_2O \rightarrow N_2 + OH \quad (R_{VII})$$
$$N_2 + O\ (+M) \rightarrow N_2O\ (+M) \quad (R_{IX})$$

seem to be due to some outlier rates, while most of the other mechanisms agree well.

These outlier rates can easily explain the behaviour observed

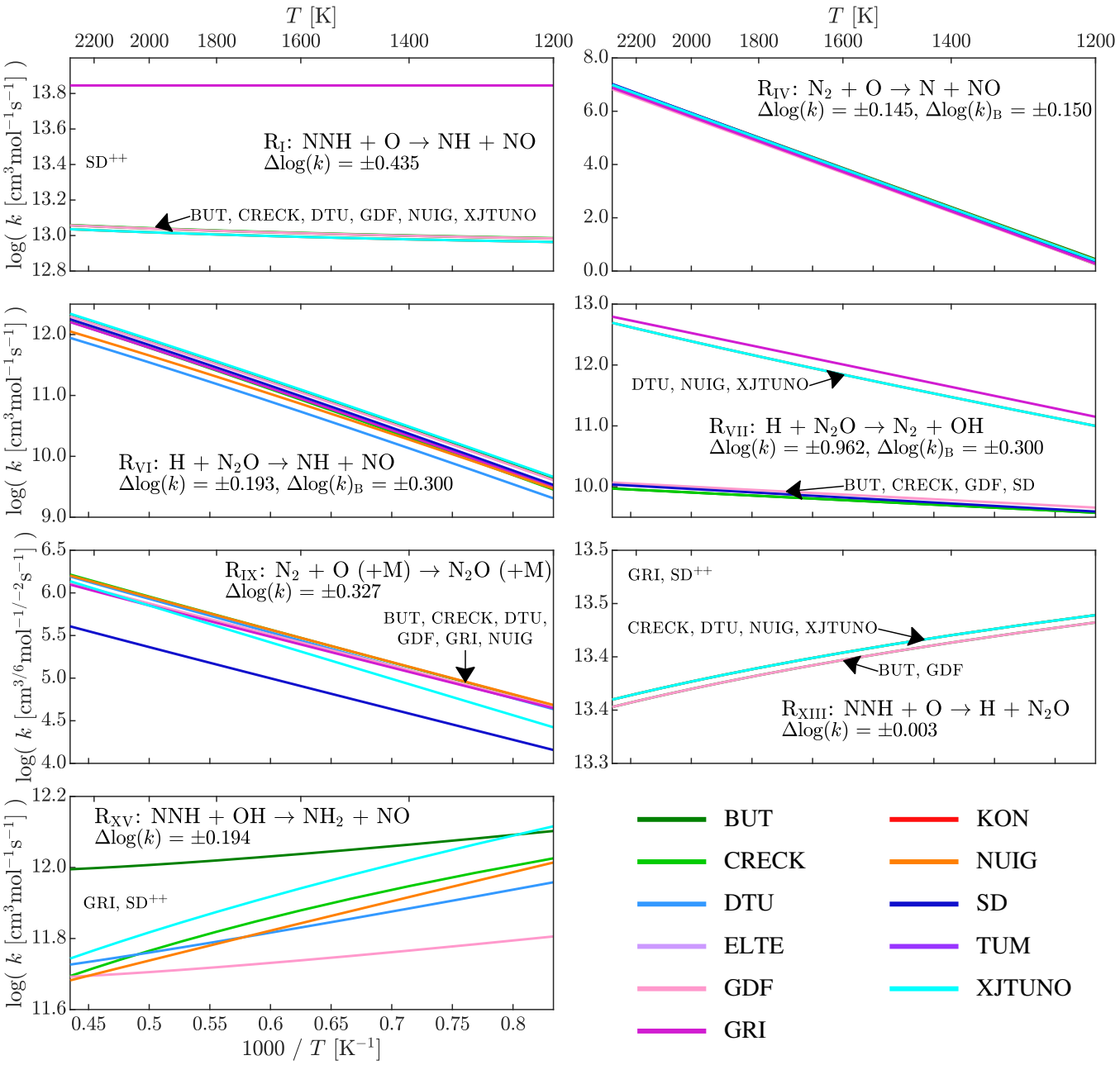

Figure 10: Arrhenius plot of the 7 NO-forming reactions identified in the sensitivity analysis. The rate is presented according to the directionality of the reaction determined using the net rate of progress of the reactions. Rates are extracted for each mechanism using Cantera at temperature from 400 K to 2300 K. The spread of the reaction rate within this temperature range is represented by $\Delta \log_{10}(k_i)$. The legend follows the colour-scale presented in Tab. 1. Please note the difference of units between bimolecular [$cm^3.mol^{-1}.s^{-1}$] and termolecular [$cm^6.mol^{-2}.s^{-1}$] reaction rates. GRI, SD^{++}: these mechanisms do not contain the reaction.

in the NO measurements for some mechanisms. GRI overestimates the rate of R_I, leading to an overprediction of the flame-front NO. Inversely, SD underestimates R_{IX}, and does not include several NNH reactions (R_I, R_{XIII}, and R_{XV}), leading to a significant underprediction of the flame-front NO. Furthermore, special attention is brought on R_{VII}, where a clear segregation is observed between the models. Several mechanisms (DTU, GRI, NUIG, and XJTUNO) are predicting a greater reaction rate than the rest of the models, and the recent mechanisms (DTU, NUIG, and XJTUNO) are using a rate coming from *ab initio* calculations performed by Klippenstein et al. [21]. This discrepancy in the rate would affect the N_2O transformation to N_2 and, therefore, reduce the N_2O contribution pathway and reduce the concentration of N_2O produced.

The study from Glarborg et al. [1] indicates that, while the models have a good agreement on most of the NO_x reactions involved in this study, this could conceal large uncertainties in their kinetic rates, especially regarding the NNH and N_2O pathways. R_I has never been measured directly and still carries large uncertainty. Similarly, R_{VI} and R_{VII} possess large uncertainty, especially at temperatures above 2200 K. Finally, according to Glarborg et al. [1], the dissociation of N_2O *via* the reverse of

R_{IX} is studied a lot, but only few measurements have been performed to measure the rate of the forward direction, leading to the observed agreement between the models (except SD) in Fig. 10 for R_{IX}.

Except for 3 reactions, R_I, R_{IX} and R_{VII}, the rest of the NO_x chemistry seems to be fairly well agreed upon between the mechanisms. Therefore, the disagreements in NO prediction between the models cannot be solely attributed to NO chemistry, and points to its interaction with the base chemistry as a more significant driver. This reinforces the significant observed impact of the hydrogen oxidation chemistry on NO predictions and implies that, without improving this, further work on optimising the NO_x sub-chemistry may yield diminishing returns.

6. Base chemistry impact on NO concentration

To fully grasp the contribution of the base chemistry in the discrepancy of the NO measurements and predictions, the mechanisms used in this study have been stripped of their NO_x sub-chemistry (except for ELTE, KON, and TUM which were already without). The NOMecha2.0 sub-chemistry [55], already discussed in the previous sections, is used as a reference in this analysis and is added to each of the base chemistries. Only GDF is not modified as it already includes NOMecha2.0, and is used as the reference in this analysis. Simulations using the 10 modified mechanisms (plus GDF) are performed using different base chemistry, but identical NO_x chemistry, such that any disagreement between the models are solely caused by disagreement within their hydrogen oxidation chemistry. It is important to note that the modification of the mechanisms is only conducted in the context of the analyses performed in the following sections. They are not intended as a direct improvement of the mechanisms, but rather to highlight the importance of the hydrogen base chemistry on the predictions of NO concentration.

Figure 11 presents the difference of NO-LIF signal predictions for the original 8 mechanisms (left) and the 10 modified mechanisms (right) for T_{ad} = 1600 K, 2000 K, and 2300 K. This shows that the use of a common NO_x sub-chemistry reduced the span of predictions that was observed in the original mod-

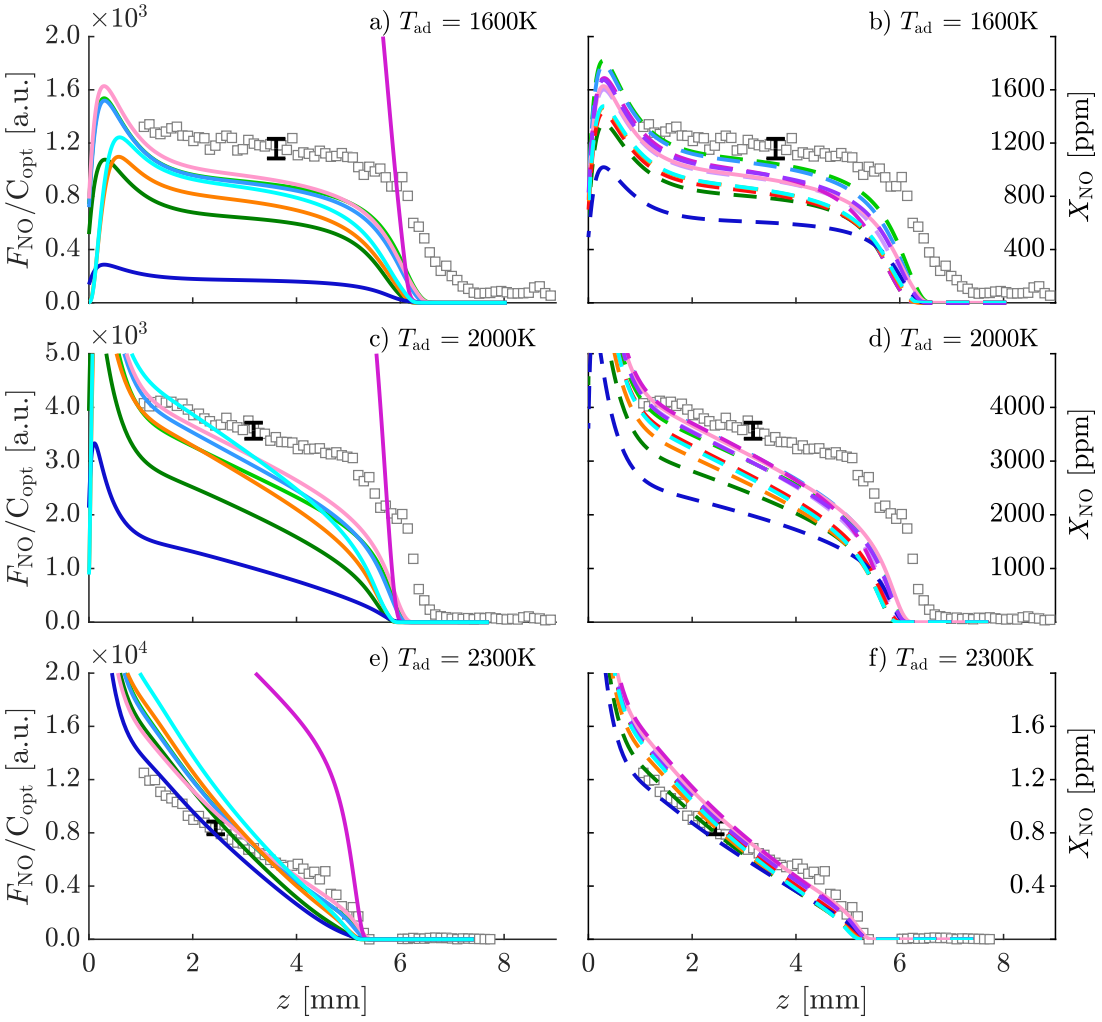

Figure 11: NO-LIF signal profiles of the flames at T_{ad} = 1600 K (top), 2000 K (middle), and 2300 K (bottom) for the experimental results (▫) and simulated results using the non-modified (—, left of the figure) and the modified mechanisms (- -, right of the figure). The legend follows the colour-scale presented in Tab. 1.

els. This indicates that some mechanisms have a NO_x sub-chemistry that is notably different from NOMecha2.0. This is specifically true for GRI and SD for which the change in NO_x sub-chemistry leads to significant improvement of the flame-front NO predictions.

Nevertheless, the same NO_x sub-chemistry does not completely remove differences in predictions between the models. In particular, the absolute flame-front NO prediction, and the predicted slope of post-flame NO formation, still vary considerably between models. These results demonstrate the impact of the different base chemistries on NO predictions.

7. Base chemistry impact on NO pathway contribution

A Reaction Pathway Analysis (RPA), which tracks atomic nitrogen, is performed to understand the impact of using a different hydrogen oxidation chemistry on the prediction of NO, whilst using the same NO_x sub-chemistry. The analysis is performed on the reference mechanism GDF, and the modified SD mechanism, referred to as SD*. These two mechanisms were chosen as they appear to be in significant disagreement regarding NO predictions at 3.5 mm from z_f (see Fig. 11b, d, and f). Tracking N-atoms describes how N_2 is broken-down to later form NO through the different NO_x pathways.

Figure 12 presents the results of the RPA performed for the flame condition at $T_{ad} = 2300$ K. The arrows represent the net fluxes of N-atoms between two species and the arrow widths are scaled with the values of the net fluxes. Coloured arrows depict the species entering (darker colour) and exiting (lighter colour) the domain. Reactive species participating in the transformation of one specie into another, in either forward or backward direction, have been added on each arrow. To simplify the

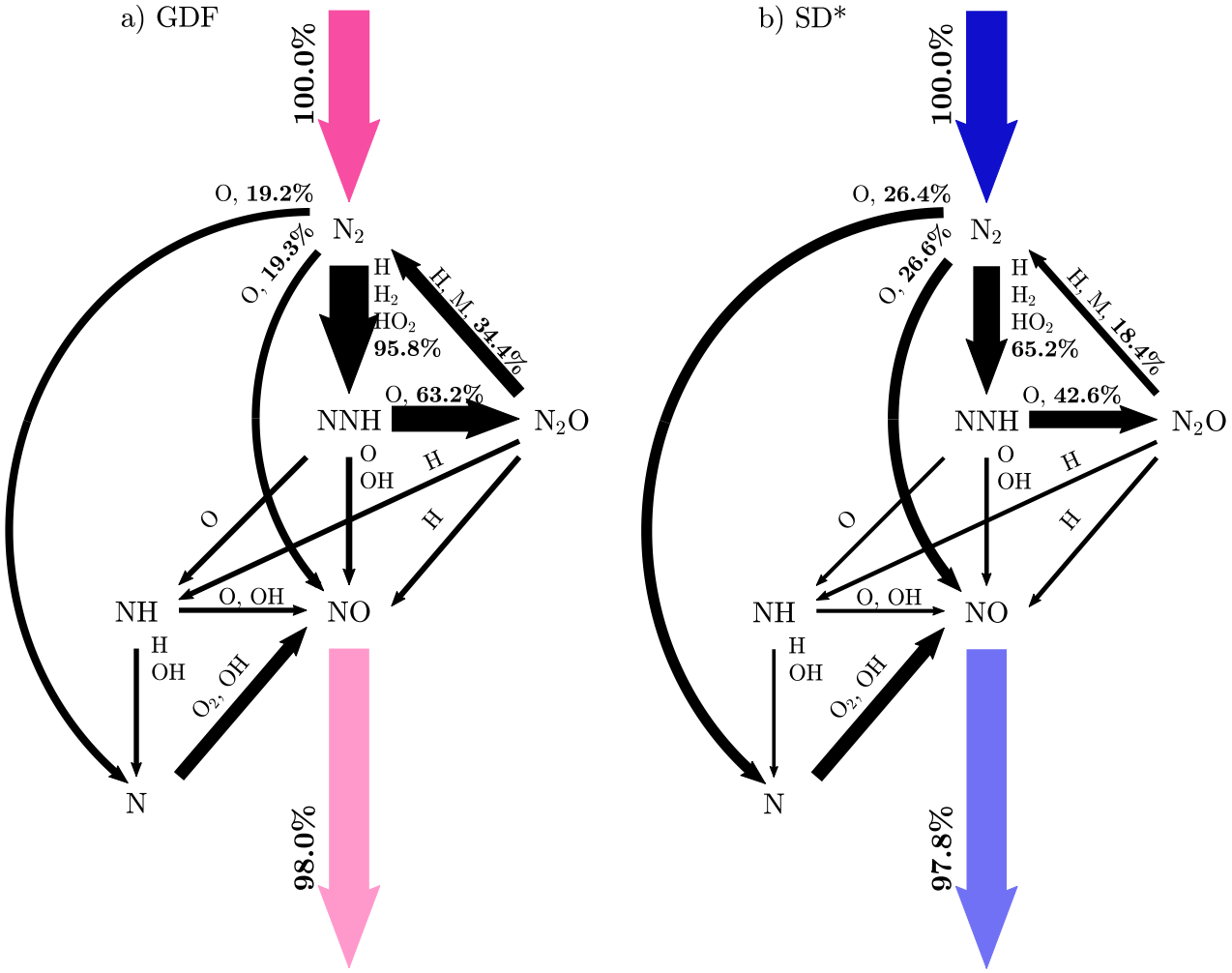

Figure 12: Reaction pathway analysis performed on atomic nitrogen at 3.5 mm from z_f, for the $T_{ad} = 2300$ K flame, using GDF (→) and SD* (→) mechanisms. The arrow sizes are scaled with the flux between two species. Only fluxes greater than 5% are shown. Reactive species participating in the transformation from one specie to another are shown and identified using the net rate of progress of each reaction. Note that the sum of the fluxes originating from N_2 to N, NO, and NNH is greater than 100% due to the recirculation loop $N_2 \rightarrow NNH \rightarrow N_2O \rightarrow N_2$.

drawing, any fluxes, species, and reactive species participating in less than 5% of the total inlet flux are not depicted. The analysis is performed for a fixed control volume and the fluxes are normalised by the N_2 entering the domain. This allows the analysis to be comparable for both mechanisms. Naturally, as both models possess the same NO_x sub-chemistry, both diagrams have the same appearance. In this comparison, it is the scaling of the arrows that is of interest.

Two main streams can be identified in this diagram: N_2 reacting through the thermal pathway and forming N and NO species, and N_2 forming NNH. The stream of N_2 forming NNH is dominant in this flame condition due to the rapid equilibrium of $N_2 + H \rightarrow NNH$ [1]. Some of the NNH species are oxidised into NO (directly or through NH), while a considerable part of NNH transforms into N_2O through R_{XIII}: NNH+O → N_2O+H. The N_2O species then either transform into NO (directly or through NH), or are reduced back into N_2. This diagram highlights the recirculation channel of $N_2 \rightarrow NNH \rightarrow N_2O \rightarrow N_2$, already identified by Durocher et al. [29]. This shows that NO production is dependent on the branching ratios of the mechanism at three points:

- $N_2 \rightarrow NNH$ versus $N_2 \rightarrow N/NO$;
- $NNH \rightarrow N_2O$ versus $NNH \rightarrow NH/NO$; and
- $N_2O \rightarrow N_2$ versus $N_2O \rightarrow NH/NO$.

By comparing this diagram to the sensitivity analysis, it is now obvious why

$$NNH + O \rightarrow NH + NO \qquad (R_I)$$
$$N_2 + O \rightarrow N + NO \qquad (R_{IV})$$
$$H + N_2O \rightarrow NH + NO \qquad (R_{VI})$$

are the most sensitive reactions for NO production (ignoring the base reactions), as they control the 3 branching ratios identified above.

It is evident that NO production is mostly dependent on the presence of O, OH, and H reactive species, as identified in the previous sections of this study. Therefore, it is clear that any difference in the hydrogen oxidation chemistry between mechanisms, will necessarily lead to differences in the predictions of NO formation through differences in the reactive species concentrations.

Comparing the GDF and the SD* analyses, it is obvious that the different base chemistry leads to differences in the contribution of the NO-formation pathways. While the overall NO production is similar for both mechanisms, the fluxes between species is significantly different. Overall, GDF predicts a stronger recirculation of N_2, stronger $NNH \rightarrow NH/NO$ and $N_2O \rightarrow NH/NO$ fluxes, but a weaker $N_2 \rightarrow N/NO$ flux. Conversely, SD* predicts a weaker recirculation of N_2, with a weaker branching ratio of $NNH \rightarrow NH/NO$ and $N_2O \rightarrow NH/NO$, but a stronger flux from $N_2 \rightarrow N/NO$. These differences in branching ratios and fluxes can be quantified by identifying the share of NO produced through the different NO-forming pathways, and is presented in the Supplementary Materials Section 6.

The difference of branching ratios between these two mechanisms appears to be uniquely controlled by the radical availability. The radical profiles for O, H, and OH are presented in Fig. 13, as well as the profile of NO concentration, for the 2300 K case. As observed, significant differences between GDF and SD* in the radical concentration profiles persist throughout the domain. These differences are more pronounced in the post-flame region, where a difference in the shape of the profiles can be observed. This observation is true for any mechanism considered in this study, a full comparison is presented in the Supplementary Materials Section 7.1 for all non-modified mechanisms. At the location of the performed RPA, the discrepancies between the two models for the OH profile reach ∼2500 ppm,

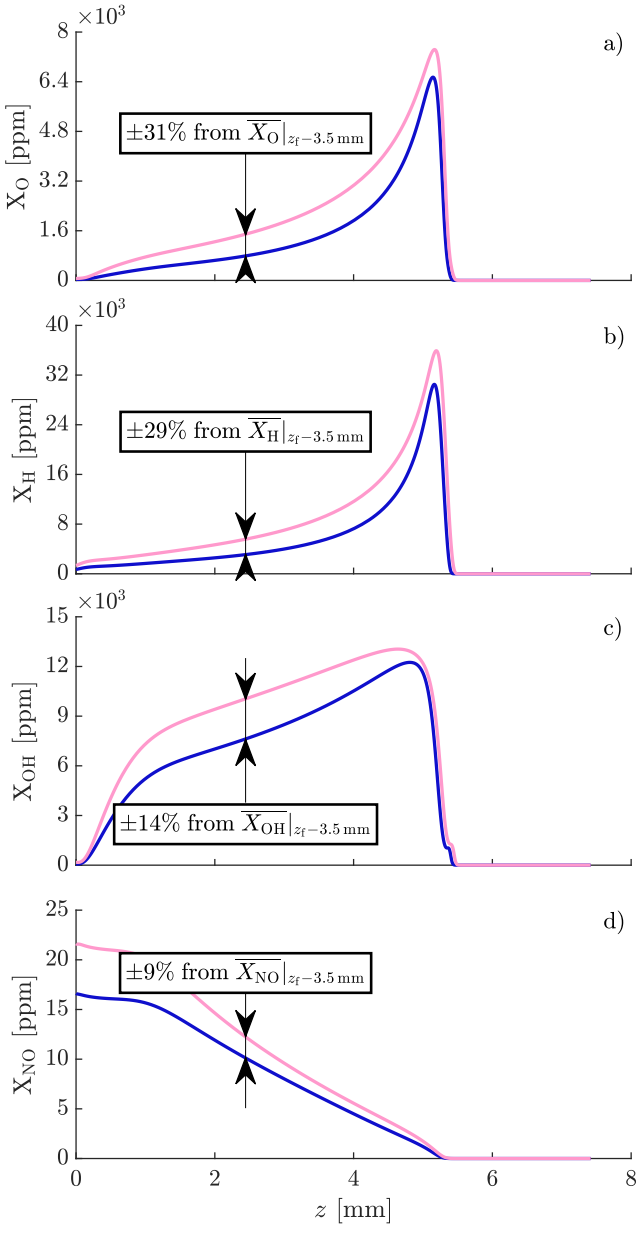

Figure 13: Numerical profiles of a) O, b) H, c) OH, and d) NO molar fraction for the flame at $T_{ad} = 2300$ K using GDF (—) and SD* (—) mechanisms.

or 14% of the average value at this location. Similarly, deltas of ∼30% can be observed in the O and H profiles at the same location. The behaviour of these profiles is indicative of a different rate of consumption/production of the radicals due to differences in the hydrogen oxidation chemistries. This impacts the NO predictions in the post-flame region, as seen in Fig. 13d.

The measurement of radical profile concentrations, on residence time scales representative of flames, would be paramount to better identify the source of uncertainty in the description of the hydrogen oxidation chemistry. Consequently, this illustrates the importance of using accurate and validated base chemistry before optimising NO_x sub-chemistries to achieve accurate NO predictions of hydrogen flames. Otherwise, prediction errors would be concealed through an overcompensation of NO-formation pathways. This also illustrates the importance of integrating time- or spatially-resolved species data, representative of practical systems residence times, in order to improve the predicting capability of the core H_2/O_2 chemistry.

8. Conclusions

In this work, nine atmospheric, stagnation, hydrogen-air flames are studied, over a wide range of adiabatic flame temperatures, to provide a set of spatially-dependent velocity, temperature, and NO concentration measurements. The stoichiometric flames are diluted with argon to reach adiabatic flame temperatures ranging from 1600 K to 2300 K. Experiments conducted using this setup, under well-controlled boundary conditions, lead to measurements with low uncertainty and high repeatability. The results of the velocity, temperature, and NO concentration measurements are compared to the prediction capability of eleven thermochemical models through 1D simulations.

Major discrepancies in the velocity prediction of the eleven models are observed at the low- and high-end temperatures. All models underpredict the reference flame speed, $S_{u,ref}$, by up to ∼20%. Better agreement can be seen at moderate temperatures from 1900 K to 2100 K, where most models predict $S_{u,ref}$ within uncertainty. This effect indicates inaccuracies in the base chemistry driving hydrogen oxidation, especially at the low- and high-end temperatures.

Predictions of NO concentration profiles by the simulations show discrepancies of several times the measured values, for both the flame-front and post-flame regions. NOMecha2.0, despite performing well in predicting NO formation in methane flames, shows poor agreement with the measurements in hydrogen flames. This suggests that the hydrogen oxidation chemistry may have a larger contribution to NO misprediction in hydrogen flames than in hydrocarbon flames.

Further analyses revealed that key reaction rates controlling O, H, and OH radicals play a major role on the velocity and NO concentration predictions and are at the origin of disagreements with the measurements. Reaction pathway analyses show that NO predictions are ultimately controlled through three branching ratios. These are uniquely controlled by radical availability, determined almost exclusively by the base chemistry used. This produces different contributions of each of the NO formation pathways, and results in an overall misprediction of NO concentration.

This study demonstrates that, no matter the optimisation process employed by the different models, major inaccuracies remain in the understanding of the H_2/O_2 core chemistry. This could be caused by a lack of hydrogen-based data in the literature, especially including time or spatially-resolved speciation profiles in flames approaching practical conditions. Therefore, this demonstrates the importance of including hydrogen-based data within the development and optimisation of models to improve hydrogen and hydrocarbon combustion modelling. Neglecting to do so will result in inaccurate NO predictions, concealed through incorrect NO formation pathway contributions driven by the radical pool behaviour defined by the base chemistry.

This work provides a robust and high accuracy NO concentration dataset, targeting a wide range of flame temperatures, performed under well controlled conditions, that could be employed for thermochemical model optimisation in order to improve their prediction capabilities in velocity and NO concentration of hydrogen flames. This would facilitate the enhancement of the performance of advanced combustion technologies and further minimise emissions from hydrogen and hydrocarbon fuelled engines.

9. Acknowledgments

The authors would like to thank the support of the National Research Council of Canada (NRC), Siemens Energy Canada Limited, the Natural Sciences and Engineering Research Council of Canada (NSERC), the Fonds de Recherche du Québéc - Nature et Technologies (FRQNT), and Climicals.

10. Supplementary Materials

Supplementary Material presents: the experimentally-measured boundary conditions and the full set of acquired experimental data, the calibration of optical constant C_{opt}, the uncertainty calculation, the NO-LIF data extraction methodology, the study of the impact of the base chemistry on the NO pathway contribution, and the radical pool profiles.

References

[1] P. Glarborg, J. A. Miller, B. Ruscic, S. J. Klippenstein, Modeling nitrogen chemistry in combustion, Progress in Energy and Combustion Science 67 (2018) 31–68.

[2] S. Park, Hydrogen addition effect on NO formation in methane/air lean-premixed flames at elevated pressure, International Journal of Hydrogen Energy 46 (2021) 25712–25725.

[3] T. Capurso, D. Laera, E. Riber, B. Cuenot, NO_x pathways in lean partially premixed swirling H_2-air turbulent flame, Combustion and Flame 248 (2023) 112581.

[4] Q. Cui, K. Morokuma, The spin-forbidden reaction $CH(^2\Pi) + N_2 \rightarrow HCN + N(^4S)$ revisited I. Ab initio study of the potential energy surfaces, Theoretical Chemistry Accounts 102 (1999) 127–133.

[5] L. Moskaleva, M. C. Lin, The spin-conserved reaction $CH + N_2 \rightarrow H + NCN$: A major pathway to prompt NO studied by quantum/statistical theory calculations and kinetic modeling of rate constant, Proceedings of the Combustion Institute, 28 (2000) 2393–2401.

[6] N. Lamoureux, P. Desgroux, A. El Bakali, J. F. Pauwels, Experimental and numerical study of the role of NCN in prompt-NO formation in low-pressure CH_4-O_2-N_2 and C_2H_2-O_2-N_2 flames, Combustion and Flame 157 (2010) 1929–1941.

[7] P. Versailles, G. M. G. Watson, A. C. A. Lipardi, J. M. Bergthorson, Quantitative CH measurements in atmospheric-pressure, premixed flames of C_1-C_4 alkanes, Combustion and Flame 165 (2016) 109–124.

[8] S. J. Klippenstein, M. Pfeifle, A. W. Jasper, P. Glarborg, Theory and modeling of relevance to prompt-NO formation at high pressure, Combustion and Flame 195 (2018) 3–17.

[9] N. Lamoureux, P. Desgroux, M. Olzmann, G. Friedrichs, The story of NCN as a key species in prompt-NO formation, Progress in Energy and Combustion Science 87 (2021) 100940.

[10] Y. B. Zeldovich, The oxidation of nitrogen in combustion and explosions, Acta Physiochimica (1946) 577–628.

[11] M. Abián, M. U. Alzueta, P. Glarborg, Formation of NO from N_2/O_2 mixtures in a flow reactor: Toward an accurate prediction of thermal NO, International Journal of Chemical Kinetics 47 (2015) 518–532.

[12] N. A. Buczkó, T. Varga, I. G. Zsély, T. Turányi, Formation of NO in high-temperature $N_2/O_2/H_2O$ mixtures: re-evaluation of rate coefficients, Energy and Fuels 32 (2018) 10114–10120.

[13] X. Han, M. Lubrano Lavadera, C. Brackmann, Z. Wang, Y. He, A. A. Konnov, Experimental and kinetic modeling study of NO formation in premixed CH_4+O_2+N_2 flames, Combustion and Flame 223 (2021) 349–360.

[14] M. Meulemans, A. Durocher, P. Versailles, G. Bourque, J. M. Bergthorson, How well do we know thermal-NO? An investigation of NO formation in flames over a wide temperature range, Proceedings of the Combustion Institute 39 (2023) 521–529.

[15] P. C. Malte, D. T. Pratt, Measurement of atomic oxygen and nitrogen oxides in jet-stirred combustion, Symposium (International) on Combustion 15 (1975) 1061–1070.

[16] G. M. Watson, J. D. Munzar, J. M. Bergthorson, NO formation in model syngas and biogas blends, Fuel 124 (2014) 113–124.

[17] A. Durocher, M. Meulemans, P. Versailles, G. Bourque, J. M. Bergthorson, Back to basics - NO concentration measurements in atmospheric lean-to-rich, low-temperature, premixed hydrogen-air flames diluted with argon, Proceedings of the Combustion Institute 38 (2021) 2093–2100.

[18] P. Versailles, A. Durocher, G. Bourque, J. M. Bergthorson, Effect of high pressures on the formation of nitric oxide in lean, premixed flames, Journal of Engineering for Gas Turbines and Power 143 (2021) 051029.

[19] M. Rieth, A. Gruber, J. H. Chen, A direct numerical simulation study on NO and N_2O formation in turbulent premixed ammonia/hydrogen/nitrogen-air flames, Proceedings of the Combustion Institute 39 (2023).

[20] J. W. Bozzelli, A. M. Dean, O + NNH: A possible new route for NO_x formation in flames, International Journal of Chemical Kinetics 27 (1995) 1097–1109.

[21] S. J. Klippenstein, L. B. Harding, P. Glarborg, J. A. Miller, The role of NNH in NO formation and control, Combustion and Flame 158 (2011) 774–789.

[22] M. S. Day, J. B. Bell, X. Gao, P. Glarborg, Numerical simulation of nitrogen oxide formation in lean premixed turbulent $H_2/O_2/N_2$ flames, Proceedings of the Combustion Institute 33 (2011) 1591–1599.

[23] A. B. Sahu, R. V. Ravikrishna, Quantitative LIF measurements and kinetics assessment of NO formation in H_2/CO syngas–air counterflow diffusion flames, Combustion and Flame 173 (2016) 208–228.

[24] J. Lee, M. C. Barbet, Q. Meng, R. E. Cornell, M. P. Burke, Experimental support for a new NO_x formation route via an HNNO intermediate, Combustion and Flame (2023).

[25] Q. Meng, L. Lei, J. Lee, M. P. Burke, On the role of HNNO in NO_x formation, Proceedings of the Combustion Institute 39 (2023) 551–560.

[26] G. M. Watson, P. Versailles, J. M. Bergthorson, NO formation in rich premixed flames of C_1-C_4 alkanes and alcohols, Proceedings of the Combustion Institute 36 (2017) 627–635.

[27] G. M. G. Watson, P. Versailles, J. M. Bergthorson, NO formation in premixed flames of C_1-C_3 alkanes and alcohols, Combustion and Flame 169 (2016) 242–260.

[28] P. Versailles, A. Durocher, G. Bourque, J. M. Bergthorson, Nitric oxide formation in lean, methane-air stagnation flames at supra-atmospheric pressures, Proceedings of the Combustion Institute 37 (2019) 711–718.

[29] A. Durocher, M. Meulemans, G. Bourque, J. M. Bergthorson, Nitric oxide concentration measurements in low-temperature, premixed hydrogen-air stagnation flames at elevated pressures, Proceedings of the Combustion Institute 39 (2023) 541–550.

[30] A. Durocher, G. Bourque, J. M. Bergthorson, Bayesian calibration of kinetic parameters in the CH chemistry toward accurate prompt-NO modelling, Journal of Engineering for Gas Turbines and Power 145 (2022) 021014.

[31] A. Durocher, M. Meulemans, G. Bourque, J. M. Bergthorson, Measurements of the laminar flame speed of premixed, hydrogen-air-argon stagnation flames, Applications in Energy and Combustion Science 7 (2021) 100028.

[32] H. J. Curran, Developing detailed chemical kinetic mechanisms for fuel combustion, Proceedings of the Combustion Institute 37 (2019) 57–81.

[33] R. C. Sausa, W. R. Anderson, D. C. Dayton, C. M. Faust, S. L. Howard, Detailed structure study of a low pressure, stoichiometric H_2/N_2O/Ar flame, Combustion and Flame 94 (1993) 407–425.

[34] J. E. Harrington, G. P. Smith, P. A. Berg, A. R. Noble, J. B. Jeffries, D. R. Crosley, Evidence for a new NO production mechanism in flames, Symposium (International) on Combustion 26 (1996) 2133–2138.

[35] G. J. Rørtveit, J. E. Hustad, S.-C. Li, F. A. Williams, Effects of diluents on NO_x formation in hydrogen counterflow flames, Combustion and Flame 130 (2002) 48–61.

[36] M. Skottene, K. E. Rian, A study of NO_x formation in hydrogen flames, International Journal of Hydrogen Energy 32 (2007) 3572–3585.

[37] R. J. Kee, J. A. Miller, G. H. Evans, G. Dixon-Lewis, A computational model of the structure and extinction of strained, opposed flow, premixed methane-air flames, Symposium (International) on Combustion 22 (1988) 1479–1494.

[38] A. C. A. Lipardi, P. Versailles, G. M. G. Watson, G. Bourque, J. M. Bergthorson, Experimental and numerical study on NO_x formation in CH_4–air mixtures diluted with exhaust gas components, Combustion and Flame 179 (2017) 325–337.

[39] R. W. Schefer, W. D. Kulatilaka, B. D. Patterson, T. B. Settersten, Visible emission of hydrogen flames, Combustion and Flame 156 (2009) 1234–1241.

[40] P. Versailles, CH formation in premixed flames of C_1-C_4 alkanes: assessment of current chemical modelling capability against experiments, Phd, McGill University, 2017.

[41] A. Durocher, Towards robust nitrogen chemistry model development: Uncertainty quantification and prediction capability in atmospheric and elevated-pressure premixed flames, Phd, McGill University, 2021.

[42] B. C. Connelly, B. A. V. Bennett, M. D. Smooke, M. B. Long, A paradigm shift in the interaction of experiments and computations in combustion research, Proceedings of the Combustion Institute 32 (2009) 879–886.

[43] J. M. Bergthorson, P. E. Dimotakis, Particle velocimetry in high-gradient/high-curvature flows, Experiments in Fluids 41 (2006) 255–263.

[44] W. G. Bessler, C. Schulz, S. Volker, J. W. Daily, A versatile modeling tool for nitric oxide LIF spectra, in: Proceedings of the Third Joint Meeting of the U.S. Sections of The Combustion Institute, Chicago, 2003, p. 105.

[45] W. G. Bessler, C. Schulz, Quantitative multi-line NO-LIF temperature imaging, Applied Physics B: Lasers and Optics 78 (2004) 519–533.

[46] G. M. Watson, J. D. Munzar, J. M. Bergthorson, Diagnostics and modeling of stagnation flames for the validation of thermochemical combustion models for NO_x predictions, Energy and Fuels 27 (2013) 7031–7043.

[47] K. K. Foo, N. Lamoureux, A. Cessou, C. Lacour, P. Desgroux, The accuracy and precision of multi-line NO-LIF thermometry in a wide range of pressures and temperatures, Journal of Quantitative Spectroscopy and Radiative Transfer 255 (2020) 107257.

[48] J. Luque, D. R. Crosley, LIFBASE Version 2.1.1, Database and spectral simulation for diatomic molecules (v1.6), 1999.

[49] K. P. Shrestha, L. Seidel, T. Zeuch, F. Mauss, Kinetic modeling of NO_x formation and consumption during methanol and ethanol oxidation, Combustion Science and Technology 191 (2019) 1627–1659.

[50] G. Bagheri, E. Ranzi, M. Pelucchi, A. Parente, A. Frassoldati, T. Faravelli, Comprehensive kinetic study of combustion technologies for low environmental impact: MILD and OXY-fuel combustion of methane, Combustion and Flame 212 (2020) 142–155.

[51] Y. Song, L. Marrodán, N. Vin, O. Herbinet, E. Assaf, C. Fittschen, A. Stagni, T. Faravelli, M. U. Alzueta, F. Battin-Leclerc, The sensitizing effects of NO_2 and NO on methane low temperature oxidation in a

jet stirred reactor, Proceedings of the Combustion Institute 37 (2019) 667–675.

[52] H. Hashemi, J. G. Jacobsen, C. T. Rasmussen, J. M. Christensen, P. Glarborg, S. Gersen, M. van Essen, H. B. Levinsky, S. J. Klippenstein, High-pressure oxidation of ethane, Combustion and Flame 182 (2017) 150–166.

[53] T. Varga, T. Nagy, C. Olm, I. G. Zsély, R. Pálvölgyi, É. Valkó, G. Vincze, M. Cserháti, H. J. Curran, T. Turányi, Optimization of a hydrogen combustion mechanism using both direct and indirect measurements, Proceedings of the Combustion Institute 35 (2015) 589–596.

[54] A. El Bakali, L. Pillier, P. Desgroux, B. Lefort, L. Gasnot, J. F. Pauwels, I. da Costa, NO prediction in natural gas flames using GDF-Kin3.0 mechanism NCN and HCN contribution to prompt-NO formation, Fuel 85 (2006) 896–909.

[55] N. Lamoureux, H. E. Merhubi, L. Pillier, S. de Persis, P. Desgroux, Modeling of NO formation in low pressure premixed flames, Combustion and Flame 163 (2016) 557–575.

[56] G. P. Smith, D. M. Golden, M. Frenklach, N. W. Moriarty, B. Eiteneer, M. Goldenberg, T. Bowman, R. K. Hanson, S. Song, W. C. Gardiner, V. V. Lissianski, Z. Qin, GRI-Mech 3.0 (1999).

[57] A. A. Konnov, Yet another kinetic mechanism for hydrogen combustion, Combustion and Flame 203 (2019) 14–22.

[58] Y. Wu, S. Panigrahy, A. B. Sahu, C. Bariki, J. Beeckmann, J. Liang, A. A. Mohamed, S. Dong, C. Tang, H. Pitsch, Z. Huang, H. J. Curran, Understanding the antagonistic effect of methanol as a component in surrogate fuel models: A case study of methanol/*n*-heptane mixtures, Combustion and Flame 226 (2021) 229–242.

[59] University of California at San Diego, Chemical-Kinetic Mechanisms for Combusiton Applications, 2016.

[60] H. Wang, N. Slavinskaya, O. Haidn, A comprehensive kinetic modeling study of hydrogen combustion with uncertainty quantification, Fuel 319 (2022) 123705.

[61] W. Sun, Q. Zhao, H. J. Curran, F. Deng, N. Zhao, H. Zheng, S. Kang, X. Zhou, Y. Kang, Y. Deng, Z. Huang, Y. Zhang, Further insights into the core mechanism of H_2/CO/NO_x reaction system, Combustion and Flame 245 (2022) 112308.

[62] D. G. Goodwin, H. K. Moffat, I. Schoegl, R. L. Speth, B. W. Weber, Cantera: An object-oriented software toolkit for chemical kinetics, thermodynamics, and transport processes, 2021.

[63] H. Wang, D. A. Sheen, Combustion kinetic model uncertainty quantification, propagation and minimization, Progress in Energy and Combustion Science 47 (2015) 1–31.

[64] J. Bell, M. Day, J. Goodman, R. Grout, M. Morzfeld, A Bayesian approach to calibrating hydrogen flame kinetics using many experiments and parameters, Combustion and Flame 205 (2019) 305–315.

[65] A. L. Sánchez, F. A. Williams, Recent advances in understanding of flammability characteristics of hydrogen, Progress in Energy and Combustion Science 41 (2014) 1–55.

[66] M. P. Burke, Harnessing the combined power of theoretical and experimental data through multiscale informatics, International Journal of Chemical Kinetics 48 (2016) 212–235.

[67] D. L. Baulch, C. T. Bowman, C. J. Cobos, R. A. Cox, T. Just, J. A. Kerr, M. J. Pilling, D. Stocker, J. Troe, W. Tsang, R. W. Walker, J. Warnatz, Evaluated Kinetic Data for Combustion Modeling: Supplement II, Journal of Physical and Chemical Reference Data 34 (2005) 757–1397.

[68] M. P. Burke, M. Chaos, Y. Ju, F. L. Dryer, S. J. Klippenstein, Comprehensive H_2/O_2 kinetic model for high-pressure combustion, International Journal of Chemical Kinetics 44 (2012) 444–474.

[69] S. J. Klippenstein, From theoretical reaction dynamics to chemical modeling of combustion, Proceedings of the Combustion Institute 36 (2017) 77–111.

[70] M. P. Burke, S. J. Klippenstein, Ephemeral collision complexes mediate chemically termolecular transformations that affect system chemistry, Nature Chemistry 9 (2017) 1078–1082.